Title
Monitoring natural gas storage using Synthetic Aperture Radar: are the residuals informative?

Journal
Geophysical Journal International, 228(2)

ISSN
0956-540X

Authors
Vasco, DW
Samsonov, Sergey V
Wang, Kang
et al.

Publication Date
2021-11-09

DOI
10.1093/gji/ggab409

Peer reviewed

Monitoring natural gas storage using Synthetic Aperture Radar: Are the residuals informative?

D. W. Vasco[1], Sergey V. Samsonov[2], Kang Wang[3], Roland Burgmann[3], Pierre Jeanne[1], William Foxall[1], and Yingqi Zhang[1]

[1] Energy Geosciences Division, Lawrence Berkeley National Laboratory, University of California, Berkeley, CA, USA e-mail: dwvasco@lbl.gov, (510) 486-5206

[2] Canada Centre for Mapping and Earth Observation, Natural Resources Canada, Ottawa, ON, Canada

[3] Department of Earth and Planetary Sciences, University of California, Berkeley, CA 94720

Summary

Estimates of line-of-sight displacements from Interferometric Synthetic Aperture Radar (InSAR) observations serve as the basis of the long term monitoring of an operating natural gas storage site at Honor Rancho in California. An inversion algorithm is used to estimate the portion of the signal that is attributable to deformation within the gas storage reservoir, located at a depth of around 3 km. Removing this contribution produces residuals that are used to characterize the background variation is surface deformation at the gas storage facility and to determine a threshold that can signify unusually large residuals. An application to almost 7 years of InSAR data, from 2011 until 2018, indicates that there are intervals of heightened residuals as well as brief episodes of anomalously large misfits. An examination of the spatial distributions of the individual residual line-of-sight displacements indicates larger displacements in an alluvial valley just south of the reservoir, with rapid spatial variations in sign, indicating a rather shallow origin. Furthermore, the two anomalous events also involve rapid spatial variations in the line-of-sight displacement residuals directly above the storage facility. The results demonstrate that the technique of extracting residuals after removing the reservoir signal is a useful approach, even in the case of this deep reservoir, and is a promising method for long-term monitoring.

Keywords: Radar interferometry, transient deformation, geomechanics, satellite geodesy

Introduction

The long-term monitoring of the movement and storage of fluids at depth within the Earth presents a number of unique challenges involving issues such as cost, temporal sampling, sensitivity, and resolution. Geophysical monitoring, in particular seismic imaging, provides high spatial resolution but is relatively expensive. Thus, full seismic surveys are not usually conducted frequently in time unless there is a permanent array in place (Hetz et al. 2020). Therefore, seismic imaging cannot typically provide the needed daily, weekly, or monthly observations necessary for long term monitoring. Micro-seismicity can be used to monitor fluid injection (Zhou et al. 2019, Carannante et al. 2020) but the relationship between seismicity and fluid movement is indirect, through the stress changes induced by the fluid injection or withdrawal (Cesca et al. 2021). Furthermore, the temporal and spatial sampling of micro-seismicity may not be favorable for field-wide evaluation. Geodetic data, that is data related to the deformation of the Earth, can be sensitive to fluid movement in the subsurface, and related events such as the displacement of fault and fracture surfaces, and can be gathered remotely using satellites (Burgmann et al. 200). This greatly reduces the cost of the monitoring, allowing for long-term operation (Ferretti 2014). Furthermore, surface deformation is very sensitive to the depth of fluid volume changes and the magnitude of the movement increases substantially as leaking fluid approaches the surface. Therefore, the monitoring of surface deformation associated with fluid injection, extraction, and storage can be used to detect leakage and otherwise anomalous behavior.

Geodetic methods for monitoring fluid flow within the Earth have a long and varied history. Some of the earliest geodetic observations were related to natural hazards, as induced by magmatic activity, and their associated large deformations. Large-scale groundwater depletion due to agricultural pumping is an early example of human induced surface deformation, drawing attention in California, as early as the 1930's (e.g., Poland and Ireland, 1975. One barrier to the detection of underlying processes, such as subsidence due to fluid withdrawal, was the lack of sensitive observations. It was only when the displacements at the surface became a serious issue, such as flooding at Long Beach California due to oil extraction at the Wilmington field (Mayugai and Allen 1969), that they garnered significant attention and organized monitoring efforts. Another example of clearly hazardous ground deformation involves the large sea floor subsidence in the North Sea at the Ekofisk field (Zaman et al. 1995), that endangered oil platforms and pipelines. In the 1990's the advent of new satellite-based remote-sensing technologies, in particular Interferometric Synthetic Aperture Radar (InSAR) that routinely measures the deformation of the Earth's surface at regular intervals, changed the situation dramatically. This development enabled cost-effective monitoring of deformation associated with geothermal field development (Massonnet et al. 1997, Carnec and Fabriol 1999), the injection of carbon dioxide into the subsurface (Yang et al. 2015), and oil and gas extraction (Fielding et al. 1998). InSAR observations also allowed for the improved characterization of surface deformation induced by groundwater pumping (e.g., King et al. 2007; Houlie et al. 2016; Chaussard et al., 2017; Ojha et al., 2019).

The geodetic monitoring of the underground storage of natural gas is a more recent development (Teatini et al. 2011) and is still a relatively rare activity. That is, of the over 600 underground gas storage sites in the world only a handful have documented monitoring efforts. Several of these are in one location, the Po Valley in Italy (Teatini et al. 2011, Jha et al. 2015, Benetatos et al. 2020). Two others are associated with the Hutubi site, the largest such facility in China, and the location of numerous earthquakes and ground motion (Qiao et al. 2018; Jiang et al. 2020). The remaining studies were conducted over a gas storage site north of Berlin, Germany (Haghighi and Motagh 2017) and in the Czech Republic (Rapant et al. 2020). All of the studies document observable surface deformation, of the order of a few millimeters to a few centimeters, that is correlated with the seasonal activity of the storage facility. One investigation by MDA Geospatial Services Inc for the Southern California Gas Company (MDA 2013) was conducted for a gas storage facility at Playa del Rey in California. Though the study did record some surface deformation over the storage area, the deformation was attributed to soil moisture changes and not to the operation of the facility. The time intervals of the study, from June to September 2012, and September to December 2012, are each less than 100 days and are too brief to capture sufficient seasonal variations attributable to the injection and withdrawal of gas. Therefore, we deem this investigation inconclusive. Even though most of those studies document the feasibility of monitoring gas storage, the small fraction of sites sampled, coupled with the rarity of leakage, mean that the effectiveness of InSAR monitoring is an open question for most sites. Furthermore, none of the previous studies present a systematic methodology for the long-term monitoring of natural gas storage.

Here we describe the application of such a systematic approach, first used in the analysis of deformation over an operating oil field, as discussed in a subsection of the paper by Vasco et al. (2017), to monitor the behavior of the Honor Rancho natural gas storage facility. Long term monitoring is warranted for natural gas storage facilities, which are often near population centers, and a handful have experienced failures in the past (Evans 2009, Conley et al. 2015). Our methodology utilizes the residuals of geodetic observations to characterize anomalous surface deformation in both space in time. The first step in this procedure is to invert the existing geodetic data for volume changes within the gas storage reservoir. Next, the volume changes are used as sources, along with a geomechanical or elastic modeling code, to calculate the predicted

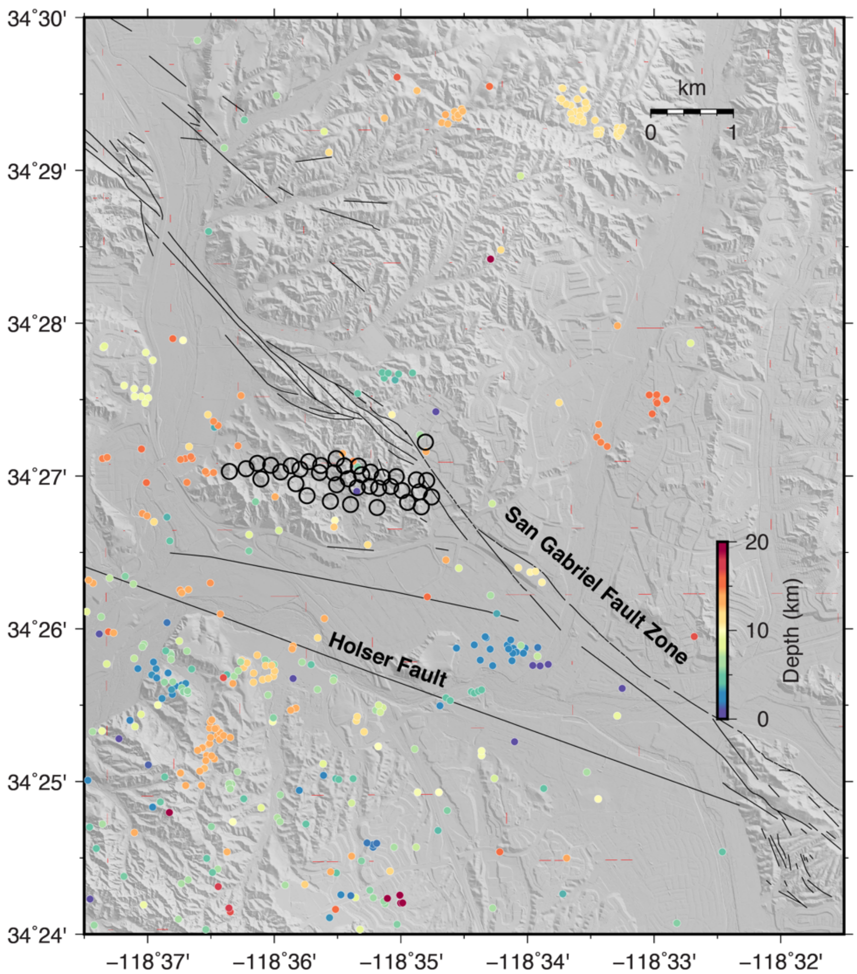

Figure 1. Geologic setting of the Honor Rancho gas storage facility, including the historical seismicity color-coded according to event depth. The locations of the intersections of the active wells with the storage interval are indicated by the open circles.

displacements due to changes within the reservoir. In this way, we remove the possible reservoir signal from the deformation data, and the residuals provide information on the non-reservoir sources of deformation. We illustrate the exact approach with an application to Interferometric Synthetic Aperture Radar (InSAR) observations from the Honor Rancho natural gas storage facility, as described below.

To be clear, we are computing the residuals from an inversion for reservoir volume change, and not based upon a full-field coupled reservoir simulation, and we feel that there are good reasons for taking such an approach. While there have been field-wide coupled simulations solving both the forward (Tenthorey et al. 2013) and inverse (Jha et al. 2015) modeling, such modeling involves the extra work associated with multiphase flow simulation within the reservoir itself. As such, it requires the specification of reservoir properties such as the porosity, permeability, relative permeability, and capillary pressure curves. The lateral variation of characteristics such are reservoir permeability can have a significant influence on the flow within the reservoir, given the non-linear nature of multiphase flow and the fact that permeability can vary by orders of magnitude. Furthermore, permeability is typically not recorded in well logs and its lateral variation is poorly constrained. In contrast, deformation within the overburden over a time interval of a few weeks to a month is largely elastic and linear, and in the absence of dramatic lateral variations in the elastic properties, is well described by smoothly-varying layers with properties obtained from well logs. So, by focusing on an inversion for volume change within the reservoir, regardless of the genesis of this volume change, we avoid the difficulty of modeling the multiphase flow within the reservoir. Thus, we reduce the number of assumptions and parameters that need to be specified. This contributes to our goal of developing a method that does not require complicated coupled modeling that is nonlinear and may not even converge. Note that, should flow properties be available and the capacity and man-power for multiphase modeling be present, one can incorporate such modeling into this methodology and compute residuals with respect to deformation driven by observed flow rates for the wells. It is even possible to modify the inverse problem to allow for perturbations in the flow rates of the flow properties in the reservoir. That could be the subject of a future publication. For this study, as noted below, we are constrained by the fact that the flow data from the wells represent co-mingled rates and we do not know the exact flow rate at each well.

Methodology and Illustration at Honor Rancho

In this section we discuss our approach for detecting unusual surface deformation, that is, ground motion that deviates from that expected during the normal operation of a storage facility. The natural gas storage facility is the Honor Rancho site, situated within the transverse mountain ranges of southern California (Figure 1). Briefly, in order to detect anomalous behavior, we first set up a geomechanical model of the reservoir and overburden and use it to remove any reservoir related ground deformation. That is, we conduct an inversion for the distribution of reservoir volume change, assuming that the observed surface deformation is due to the injection and withdrawal of natural gas. The residuals, the component of the surface deformation that cannot be explained by volume changes within the reservoir, are then used to determine the background variability or natural noise in the surface deformation. Significant deviations from the usual background noise can then be used to define anomalous events that may signify leakage, or should at least prompt a closer examination of the residuals and their spatial distribution. We shall describe each step of this approach in more detail in the sub-sections below.

Monitoring of Surface Motion using Interferometric Synthetic Aperture Radar (InSAR)

InSAR methods rely on the phase delay of a reflected microwave or radar wave to estimate the displacement of points on the Earth's surface (Bürgmann et al., 2000; Ferretti 2014). As discussed below, the phase shifts of the reflected pulses can be used to estimate the changes in distance along the line-of-sight (LOS) direction of the satellite. Satellite-based InSAR systems have been available since the late 1990's and have proliferated since the mid-2000's. These systems have different characteristics, such as re-visit times, cost, radar central frequency, and the look direction. For example, Sentinel-1 data from the European space agency are available at no cost.

The literature on InSAR techniques and applications is vast and many techniques have been developed to improve the calculation of range change (e.g. Bürgmann et al., 2000; Osmanoğlu et al., 2016). Two of the more promising approaches that have led to estimates of surface deformation with millimeter-level precision are small baseline subset (SBAS) analysis (e.g. Berardino et al., 2002; Schmidt and Bürgmann, 2003) and permanent or persistent scatterer (PS) techniques (e.g. Ferretti et al., 2001, Hooper et al. 2008, Hooper et al. 2012). Both methods use a sequence of interferograms to overcome the limitations of conventional InSAR analyses, namely: phase decorrelation, which involves possible significant changes in the radar signature over the area of interest related to thick vegetation, ice/snow cover, high rate of surface deformation, rugged topography, and atmospheric effects such as strong precipitation. Both of these methods are discussed below, in reference to monitoring at the Honor Rancho gas storage facility.

To better understand the small baseline and persistent scatterer approaches, we need to consider the nature of InSAR observations and the factors contributing to phase delays. To this end, consider the phase of a pulse reflected from a point on the Earth, a single pixel in a SAR image. The phase value φ of a pixel P of a radar image can be modeled as a mixture of four distinct contributions (Ferretti 2014):

$$\varphi(P) = \vartheta + \frac{4\pi}{\lambda} r + a + n \quad (1)$$

where ϑ is the phase shift related to the location and to the reflectivity of all elementary scatterers within the resolution cell associated with pixel P; λ is the radar wavelength; r is the distance between the satellite and the pixel on the ground; a is the propagation delay introduced by variations in the Earth's atmosphere between image acquisitions, and n is the phase contribution related to the system noise such as thermal vibration of the radar system and co-registration. The term $4\pi r/\lambda$ is the largest contribution in any geodetic application, as it is associated with the sensor-to-target distance or range, r. The phase values contained in a single SAR image are of little practical use, as it is impossible to separate the different contributions in equation (1) without prior information. The basic idea of SAR interferometry is to measure the phase *change*, or interference, over time, between two radar images, generating an *interferogram* I:

$$I = \Delta\,\varphi(P) = \Delta\,\vartheta + \frac{4\pi}{\lambda}\Delta r + \Delta a + \Delta n \quad (2)$$

If we consider an idealized situation where the noise is negligible, the surface character and atmospheric conditions are constant between the two SAR acquisitions, the satellite's orbits and the surface topography are precisely known (which are necessary to compute the term $\Delta\,\vartheta$), then equation (2) reduces to

$$I = \Delta\,\varphi(P) = \frac{4\pi}{\lambda}\Delta r. \quad (3)$$

Therefore, if a point on the ground moves during the time interval between the acquisition of the two radar images with similar geometry, the distance between the sensor and the target changes, creating a phase shift proportional to the displacement. When multiple SAR acquisitions are available, one can form a sequence of interferograms satisfying certain conditions (e.g., a limit on the maximum spatial and temporal baselines), and construct the time series of surface deformation at the SAR acquisition times. We note that the two methods, SBAS and PS, can both be used for time series analysis, but they differ in how they mitigate phase decorrelation for robust phase unwrapping and other operations, such as atmospheric noise reduction.

Analysis of RADARSAT-2 InSAR Observations using the Small Baseline Subset method

The Small Baseline Subset (SBAS) method (Berardino et al., 2002, Lanari et al. 2004, Hooper 2008, Samsonov et al., 2011, Samsonov and d'Oreye 2012) selects many coherent interferograms acquired with minimal spatial and temporal differences between two satellite passes, and then solves for the deformation rates between subsequent SAR acquisitions, reconstructing the time series of the cumulative displacements. The spatial baseline is the distance between the satellite positions as they sample a point on the Earth's surface. The distance is measured in the direction perpendicular to the look direction, a vector pointing toward the point on the Earth's surface. The temporal baseline is

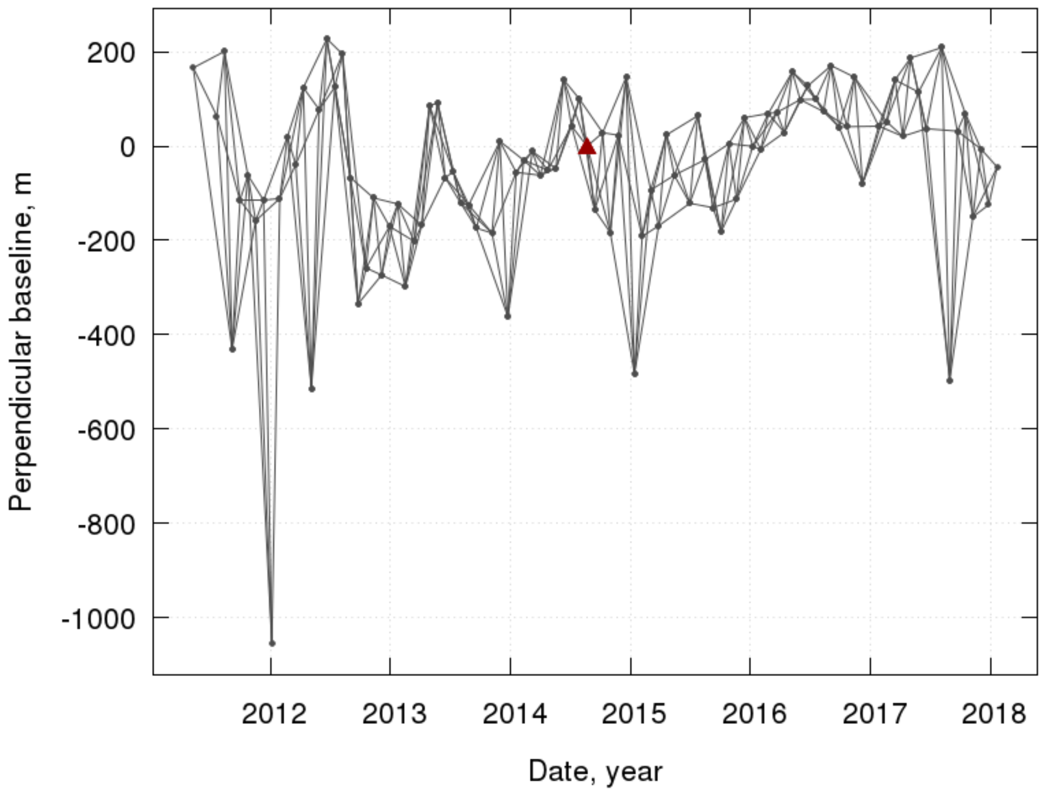

Figure 2. Temporal and spatial baselines for RADARSAT InSAR data. Each line represents an interferogram showing the time span and orbit-perpendicular separation (in meters) of the two image acquisitions. The red triangle indicated the reference epoch used in the time series generation.

the time interval between the two satellite passes. In the small baseline approach orbits for which both of these measures are small are used to derive corrections and parameters for extracting reliable time series of line-of-sight displacement. For our analysis at Honor Rancho, we utilized ascending orbit observations from the RADARSAT-2 system operated by the Canadian government. The azimuth of the orbit is 348 degrees and the incidence angle for observing the line-of-sight displacement is 28 degrees. A repeat time of 24 days allows for nearly monthly observations. The precision of the estimates of surface displacement, in this case in the direction of the satellite position as it samples the area, is of the order of 0.5 cm relative to a reference point in the area of interest. A reference point was used for the processing and a new reference point was chosen in an area that seemed to be in a stable area of the scene. InSAR data from early 2011 until the start of 2018 were used in the field testing of the approach for detecting anomalous events. The Small Baseline Subset (SBAS) technique was used to obtain estimates of range change, a change in the distance to the satellite for all of the time intervals for this period. The variation in temporal and spatial baselines of the interferograms used in this analysis are shown in Figure 2 for the time interval that we considered. The image pairs that are close in space and time, as indicated in Figure 2, are used to estimate corrections such as uncompensated topography. Application of the SBAS method produced estimates of range change for a large area encompassing the Honor Rancho gas storage facility. Line-of-sight displacements indicate movements exceeding 4 cm over the entire seven-year period (Figure 3). The area displays a complicated pattern of deformation with some evidence of tectonic displacements and indications of subsidence and uplift associated with numerous oil fields in the region. We will focus on the area around the Honor Rancho gas storage facility, indicated by the unfilled circles, in greater detail below, when we compare estimates of displacements provided by SBAS and permanent scatterer analyses.

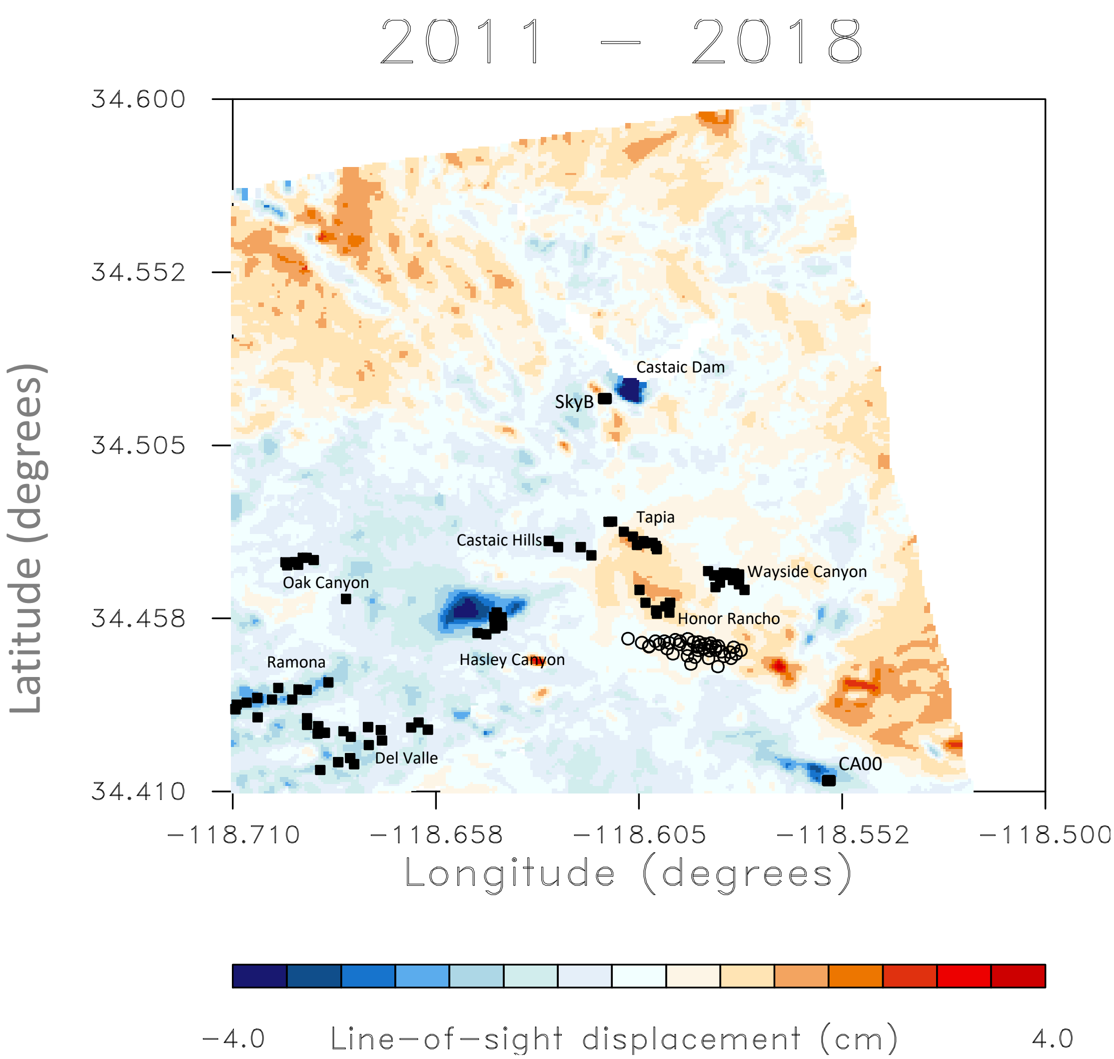

Figure 3. Line-of-sight displacements in the region around Honor Rancho. Active oil wells associated with several nearby fields are indicated by the filled squares and labeled fields. The Honor Rancho field gas wells are denoted by the open circles. The dark blue, indicating subsidence just to the north of the center of the region is likely due to hydrological changes around a secondary lake just to the south of Castaic dam. Two GPS stations, SkyB and CA00 are indicated by the filled squares and labels.

Analysis of Sentinel-1 InSAR Observations using the Persistent Scatterer Technique

The second method that we employed relies upon the identification of point-wise, coherent, radar targets, often referred to as permanent or persistent scatterers (Ferretti et al. 2001; Hooper et al. 2004). In particular, persistent scatterer techniques (Ferretti et al. 2001, 2011) identify pixels with stable properties and focus the processing on these permanent scatterers. Restricting our attention

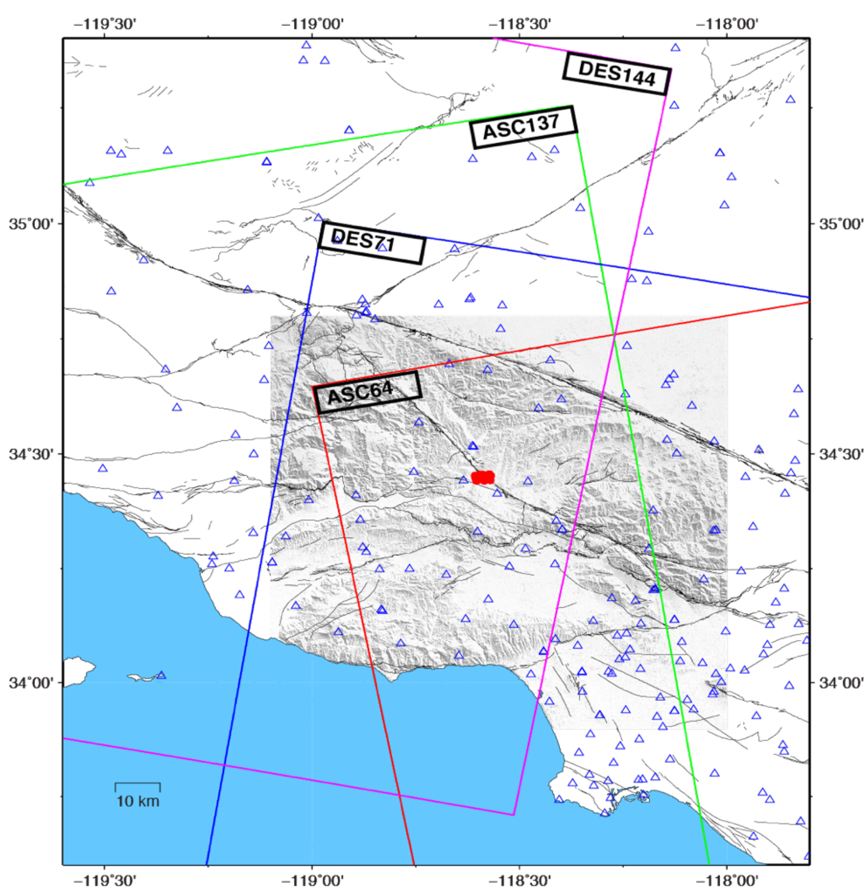

Figure 4. Coverage of InSAR observations over the Honor Rancho gas field. The footprint of SAR image of each satellite track is shown as color lines. Red circles show the wells in the gas field. The blue triangles represent the Global Positioning System (GPS) sites in southern California. Note that there are no GPS sites in the immediate vicinity of the gas field.

to scatterers with stable properties facilitates the phase unwrapping and removal of atmospheric noise through a combination of temporal and spatial filtering (Hooper et al. 2008). The accuracy of InSAR measurements depend upon a variety of factors including spatial (distance between subsequent satellite passes) and temporal (time span between two acquisitions) baselines, radar wavelength, land cover, and atmospheric conditions. First, we geometrically aligned the images to a single reference image and generated the corresponding reference and secondary interferograms with GMTSAR (Sandwell et al., 2011; Xu et al., 2017). No filtering was applied at the stage of making the interferograms. We used the StaMPS software, version 3.3, with default parameters to perform the permanent scatterer analysis (Hooper et al. 2004; 2007). Further details of the Sentinel-1 PS analysis can be found in Wang and Fialko (2018).

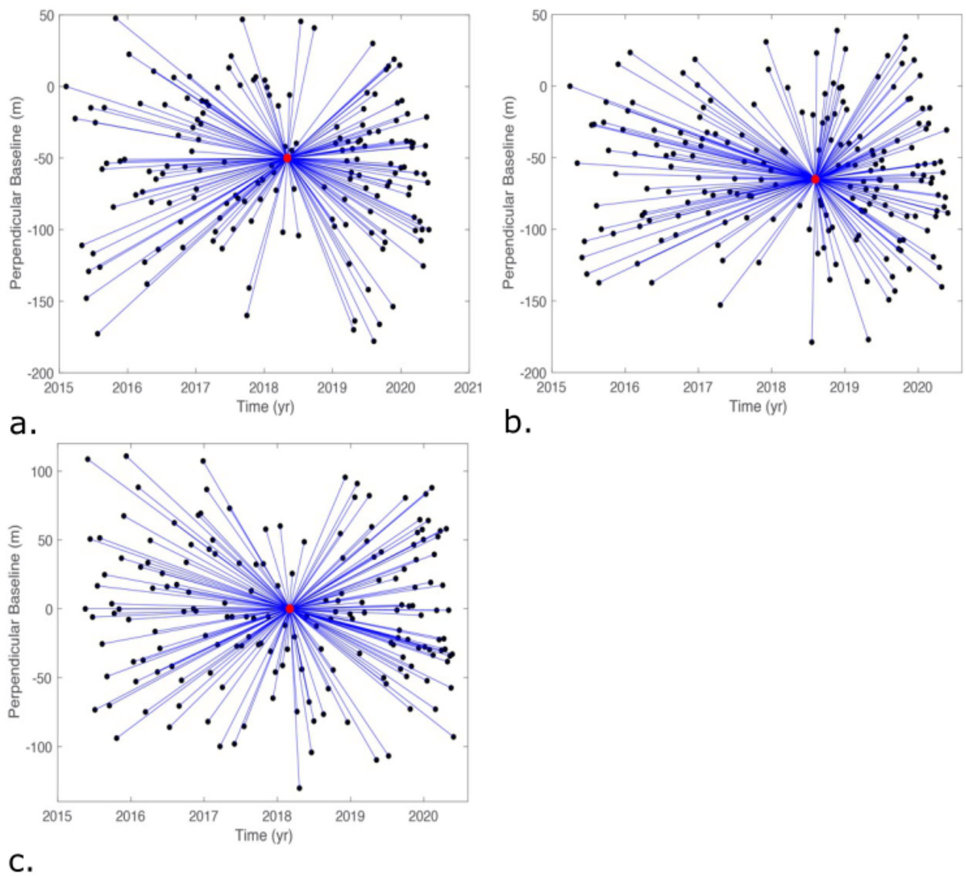

Figure 5. Perpendicular baseline distribution of Sentinel-1 SAR for track ASC64 (top left), ASC137(top right) and DES144 (bottom left). Red and black dots represent reference and secondary images to form the interferograms.

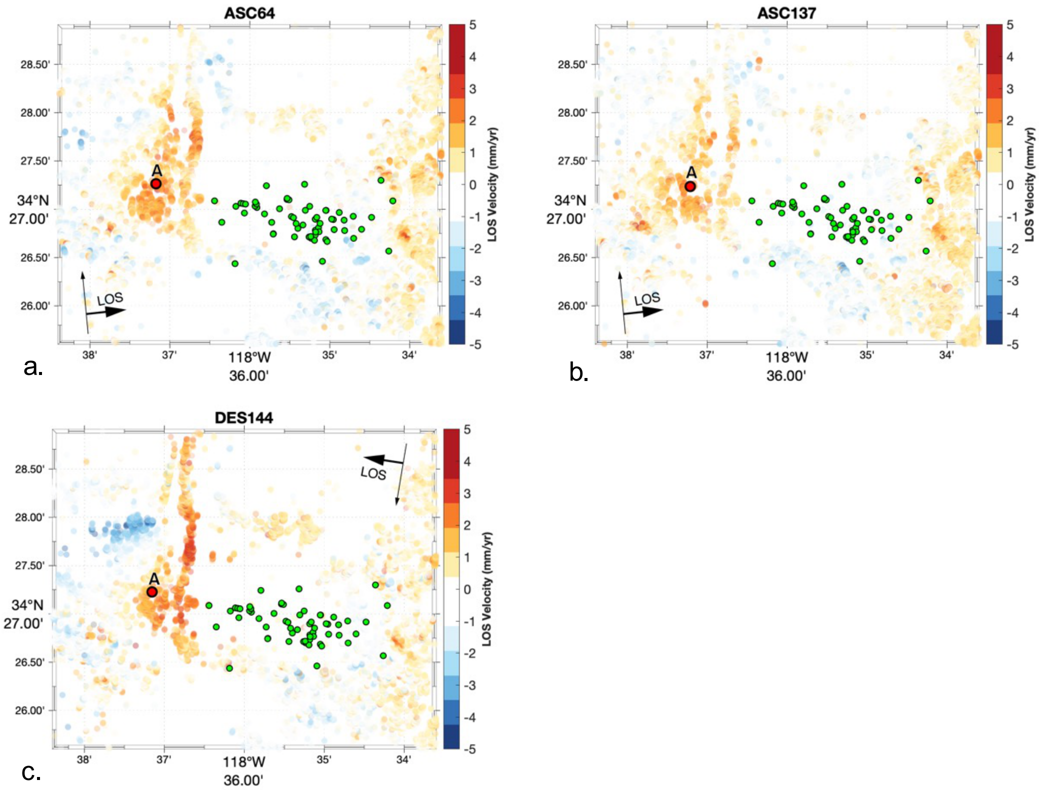

Figure 6. Sentinel-1 Line-of-sight (LOS) velocity of ground motion around the Honor Rancho gas field. Green circles show the well distributions. Positive values correspond to surface motion toward the satellite (i.e. uplift if all movement is vertical). The time series at point A are shown in Figure 7.

There are four Sentinel-1 satellite tracks covering the Honor Rancho gas field from different view geometries (Figure 4). In this study, we processed data from three tracks: ASC64, ASC137 and DES144 from the middle of 2015 to June 2020. Image acquisitions over the study area can be divided into three phases. From 2015 to the middle of 2016, the intervals between image acquisitions were mostly 24 days, which were reduced to 12 days starting from early 2016 when Sentinel-1B was launched, and 6 days starting from early 2018. From April 2015 to June 2020, there are 164, 193 and 178 acquisitions for tracks ASC64, ASC137 and DES144, respectively, which completely cover the study area. The two ascending tracks (64 and 137) and one descending track (144) were examined independently to produce three estimates of time-varying range changes for the Honor Rancho area. The spatial and temporal baselines for the descending track DES144 and the ascending tracks ASC64 and ASC137 are shown in Figure 5. The estimated line-of-sight velocities for a time interval extending from early 2015 until the beginning of 2019 are shown for the identified scatterers of the three tracks

(Figure 6). All three tracks contain an area of apparent uplift (range decrease) just to the west of the Honor Rancho field, extending in a roughly north-south direction.

Figure 6 shows the average line-of-sight (LOS) velocity of persistent scatterers derived from Sentinel-1 observations around the Honor Rancho gas field. As most of the wells are distributed in between ridges, only a limited number of persistent scatters (PS) are found in the immediate vicinity of the gas field. High-quality persistent scatters are identified 1-2 km west of the Honor Rancho well field, where the LOS velocities of all three tracks are characterized by a range decrease of 3-5 mm/yr during the observation period from 2015 to 2020. Given that data from the three tracks are acquired at different times from different view geometries, the inferred range changes in this area are unlikely to be due to processing artifacts or noise, such as residual atmospheric noise. Instead, we believe that they reflect true surface deformation, primarily uplift, in this area. In order to gain a better understanding regarding the nature of this uplift, we considered the temporal variation for scatterers in roughly the same position, indicated by the red circles and the letter A in Figure 6. The time-varying line-of-sight displacements for image pixels at point A are plotted in Figure 7. While all three of the time series display significant temporal variability, which may be due to natural cycles such as rainfall or variations associated with the Honor Rancho field or another oil and gas field, there is also a systematic jump in the line-of-sight displacement starting at the beginning of 2017. This rapid change is particularly evident in the displacements for ascending track 64 (ASC64) and the descending track 144 (DES144).

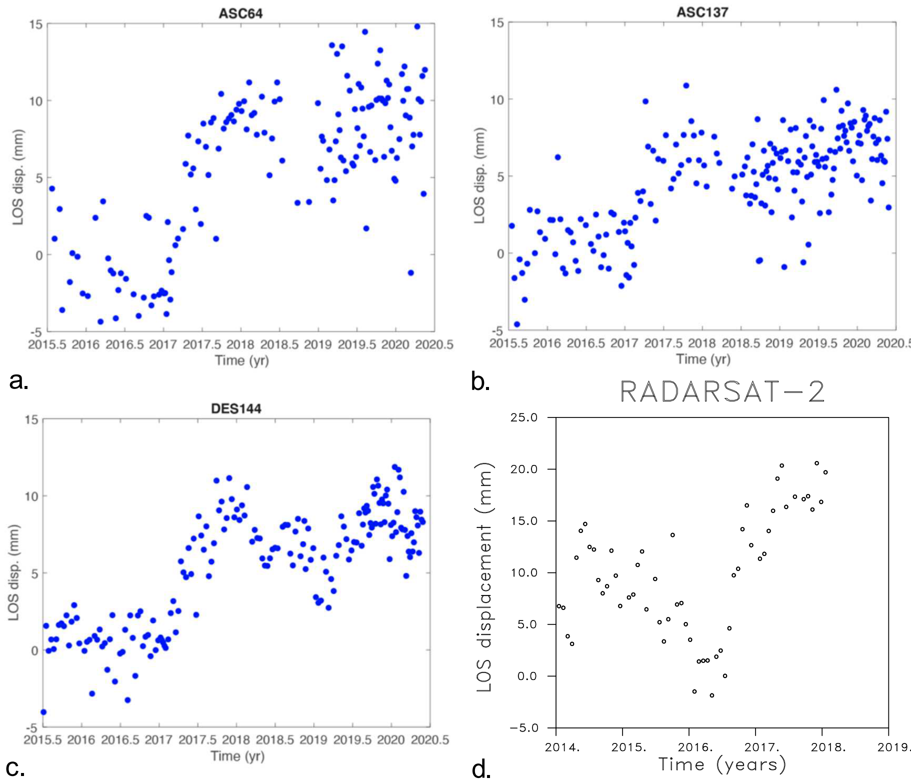

Figure 7. (a.-c) LOS displacement time series at a point west of the gas field, as marked by the red circle in Figure 6. (d) Corresponding displacements for the same point extracted from RADARSAT-2 data. Note the different time interval for the RADARSAT-2 data.

The cumulative line-of-sight displacement associated with this jump is 6-7 mm. The increase in the line-of-sight displacement is also seen in the RADARSAT-2 data (Figure 7), though the time sampling is not equivalent to that of the Sentinel 1 observations. The permanent scatterer analysis of the Sentinel 1 data in this study did not yield a dense distribution of persistent scatters in the immediate vicinity of the wells, making it hard to assess if any of the observed surface deformation in this area is directly related to the gas storage operation.

A Comparison of RADARSAT-2 and Sentinel-1 Interferometric Synthetic Aperture Radar Observations

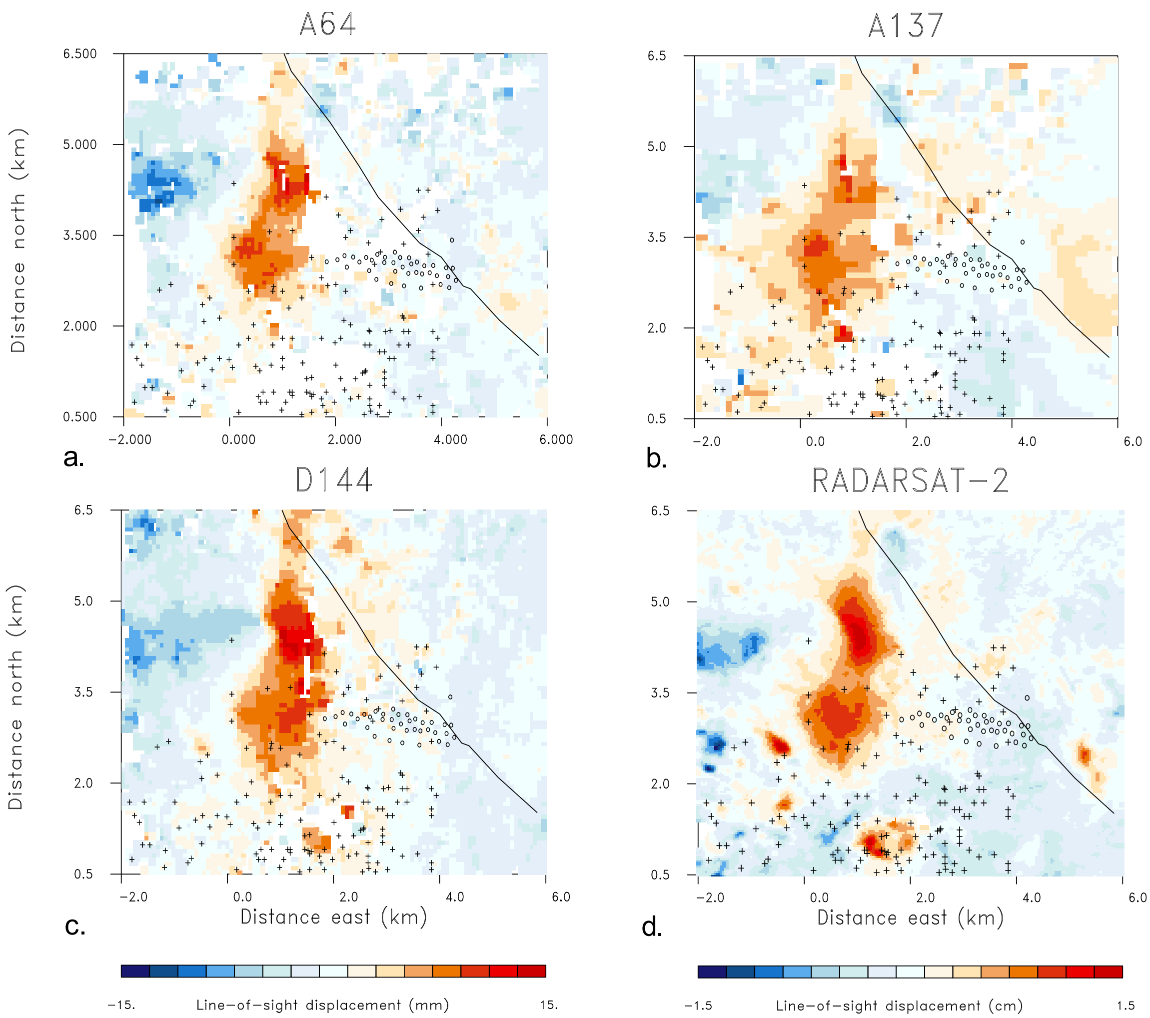

Figure 8. Comparison of cumulative LOS displacement (from 2016 to 2018) derived from Sentinel-1 and RADARSAT-2 data. Positive values correspond to surface motion toward the satellite (uplift if all movement is vertical). The titles indicate the Sentinel 1 track and are labeled A for ascending and D for descending. The RADARSAT-2 data is from an ascending orbit with an azimuth of 348 degrees and an incidence angle of 28 degrees. The open circles signify wells at the Honor Rancho natural gas

As noted above, the Small Baseline Subset (SBAS) method is quite different from the permanent scatterer (PS) technique and it is worthwhile comparing the two methods and their estimated displacements for the Honor Rancho area. Furthermore, the RADARSAT-2 satellite properties differ from those of the Sentinel-1 monitoring system but they should both detect surface movement in the region. In order to make a more detailed comparison around the gas storage facility, we considered line-of-sight displacements estimates from both the SBAS results of RADARSAT-2 and PS results for the three Sentinel-1 tracks. To account for the differences in spatial sampling and time intervals, we constructed data averages utilizing spatial and temporal bins. In particular, a 7.0 km by 6.5 km area around the Honor Rancho natural gas storage area was divided into a 125 by 100 grid and line-of-sight displacements were averaged within each bin to compute a mean value. If there were less than 3 estimates within a grid block, the average was discarded and no value was given for that area. Furthermore, a common time interval from January 2016 until January 2018 was used to compute the total or cumulative line-of-sight displacement. The resulting averages, shown in Figure 8, indicate fair agreement, between the results of three Sentinel-1 tracks (A64, A137, and D144), based on the persistent scatterer analysis and RADARSAT-2 results based on SBAS. The deformation during this two-year period is dominated by the uplift to the west of Honor Rancho mentioned earlier. This uplift occurs within the Castaic Creek drainage basin, downstream from the Castaic Dam and may be due to abundant rainfall in late 2016/early 2017. This is supported by the time series plotted in Figure 7, which document rapid uplift in early 2017 when the rainfall is most significant. While there are no

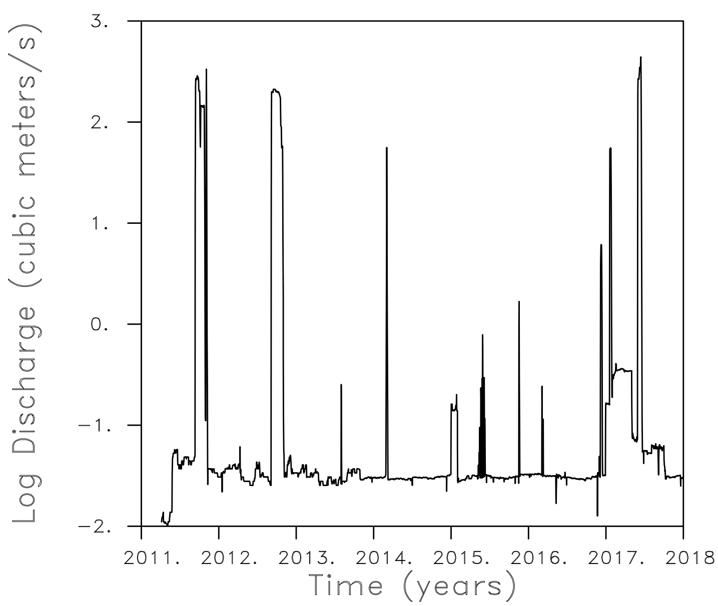

Figure 9. Volume of discharge from Piru Creek, which lies a short distance to the west of Castaic Creek. Data from the U.S. Geological Survey [https://waterdata.usgs.gov/nwis]

observations of discharge at the Dam or Castaic Creek, observations of flow discharge from the nearby Piru Creek below the Santa Felicita Dam (Figure 9) indicate a large and sustained increase in early 2017. In addition, the water level of the Castaic dam reached a maximum during this time, making large releases much more likely. Thus, the most plausible explanation of the uplift in Figure 8 is due to hydrological factors, although this cannot be demonstrated conclusively. Note that no large secular trend of displacement is observed directly over the gas storage site, suggesting no directly related deformation, at least during this time interval. The pronounced subsidence at the very western edge of the area in Figure 8 is likely due to operations at the Hasley Canyon oil field which is labeled in Figure 3.

A Comparison with Data from the Global Positioning System

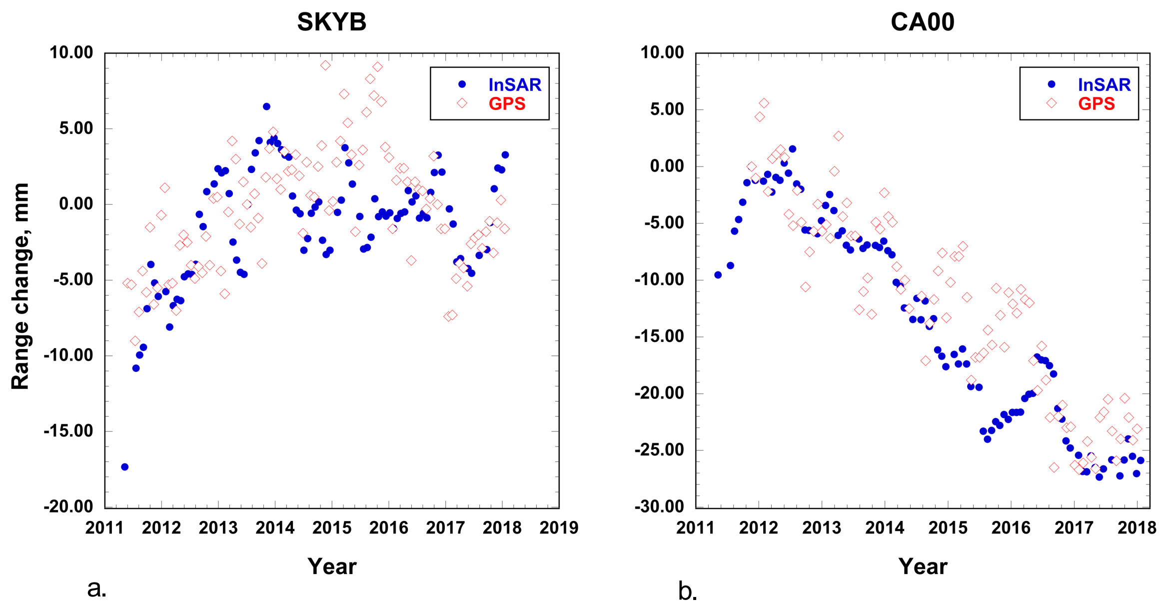

Figure 10. Comparison of InSAR range change and GPS estimates of range change. (a). Map showing the location of the two GPS instruments with respect to the Honor Rancho gas storage site. (b) Range change time series estimated using GPS displacement observations, compared with InSAR estimates.

In order to validate the RADARSAT-2 SBAS estimated line-of-sight displacements, we compared these data to observations of three-dimensional displacement time series from nearby Global Positioning System (GPS) stations. There are two stations in the general vicinity of the Honor Rancho gas storage site with time series covering the time interval of interest: SkyB and CA00 (Figure 3). Examining the time series in for both the InSAR and GPS, plotted in Figure 10, one observes the significant variation in the range change with location in the region. The GPS instruments give all three components of displacement of points on the Earth's surface. Using the line-of-sight to the satellite, we projected the displacement vector onto the look vector to obtain estimates of range change for each instrument as a function of time. In Figure 10 we compare the RADARSAT-2 InSAR range change estimates at each GPS site obtained by piecewise polynomial interpolation. There is general agreement between the two data sets. There is considerable scatter in the range change estimates, though the systematic changes at CA00 are substantially larger than the scatter or noise at the station.

Identifying Anomalous Events

A long-term gas storage monitoring system should flag unusual behavior in a relatively automatic fashion and, once it is operational, should only require expert intervention after the detection of an anomalous event. With this in mind we developed a method for classifying observed displacements

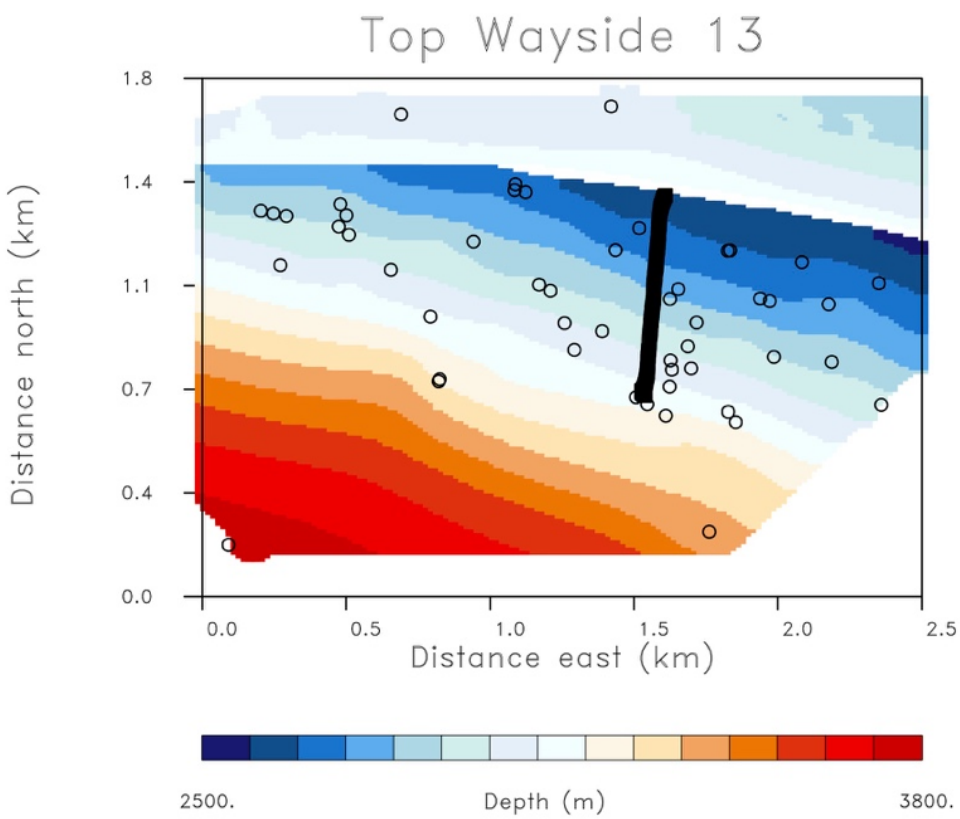

Figure 11. Top boundary of the gas storage interval at Honor Rancho. The well head locations are plotted as open circles. The line of filled squares signify the horizontal projection of the path of the well containing the compressional and shear sonic logs used to construct an elastic model of the overburden.

as either routine or anomalous. Summarizing this process, we use the InSAR observations described above to estimate the volume changes in the gas storage reservoir that best explain the observed surface deformation over a given time interval. These estimated volume changes are then used to calculate the deformation due to the reservoir processes and this calculated displacement is then removed from the observations. The residual deformation, with the reservoir signal removed, is then used to define normal and anomalous behavior. Specifically, we consider a long time series of InSAR data and use the time-varying residuals to determine the natural or background variation in the InSAR measurement errors and the surface movement. Anomalous events are then defined as episodes during which the residuals substantially exceed this natural background variation. These ideas should become clearer as we describe and illustrate the approach using data from the Honor Rancho gas field.

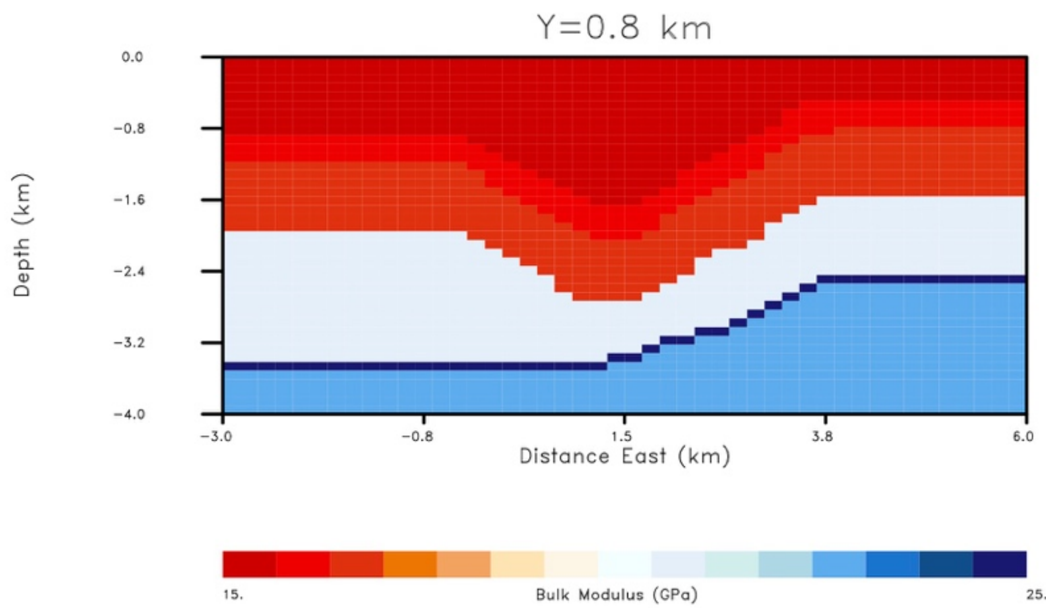

Figure 12. East-west cross-section (at north distance of 0.8 km in Fig. 11) through the top portion of the elastic model derived using the boundaries derived from well intersections and the elastic properties from the log in the well shown in Figure 11. The reservoir interval corresponds to the thin dark blue layer near the base of the model.

The first step is to calculate the residuals and that requires a geomechanical model of the reservoir-overburden system for both forward and inverse modeling. Using the reservoir layer boundaries determined by the numerous well intersections in the field we can define the reservoir top and bottom (Figure 11) as well as the interfaces defining the major layers composing the overburden. In this manner we can construct a fully three-dimensional elastic model describing the reservoir, the overburden, and the under-burden. A vertical slice through the top 4 kilometers of this model is plotted in Figure 12. Furthermore, one well was logged throughout the overburden and through the reservoir, providing compressional and shear sonic velocities and densities from the surface to below the reservoir. These variations were averaged over the layers of the model to provide estimates of the dynamic moduli associated with each major formation. The surface trace of the curving well is plotted in Figure 11. An east-west cross-section through the model (Figure 12) highlights the depth variation of the main layers in the model. The reservoir is the thin dark-blue layer in the figure. In regions away from the gas storage facility, where there are few or no wells and we have little or no information about the formation geometry, we assume flat-lying layers.

Changes in the fluid volume within the reservoir, due to gas injection and withdrawal, lead to variations in the effective pressure, that is the difference between the total pressure and the fluid pressure, introducing stress changes within the reservoir and its surroundings. Under favorable conditions, such as a deformable reservoir and surface conditions that do not change significantly in time, the resulting stress and strain leads to observable surface deformation. To make use of these observations, if available, we need to relate the surface deformation to reservoir processes. There are several levels of sophistication that can be used to describe this relationship. At the simplest level, we can relate the surface deformation directly to reservoir volumetric change, without calculating the fluid pressure changes that led to the volume change. Thus, we restrict ourselves to purely mechanical considerations and are not concerned with the modeling of the fluid flow leading to the volume change. This approach involves the fewest model parameters, and if we are interested in short time intervals, can usually be accomplished using an elastic or a poroelastic model for the overburden (Vasco et al. 2010). More sophisticated simulations of the fluid flow within the reservoir can also improve the fidelity of the modeling, at the expense of introducing additional, often unknown, parameters such as reservoir permeability and porosity. The most advanced modeling involves consideration of both the fluid flow and the deformation using a coupled numerical simulator (Rutqvist 2011). This comprehensive approach requires additional information, such as the reservoir flow properties, and further characterization of the reservoir. In order to simplify the monitoring, we do not take the additional step of fluid flow modeling, adopting a purely mechanical methodology, as described in Vasco et al. (2017).

The conceptual model that we use to relate the deformation to reservoir volume change is similar to that applied in seismic source estimation and imaging. That is, though the source volume may undergo non-linear deformation and strain, the much smaller deformation outside of the source region can be described using methods from linear elasticity over the time interval between surveys, typically less than one month. In particular, one can use a Green's function, $G_i(\mathbf{x}, \mathbf{y})$, or elastic impulse response function, relating the displacement of the overburden $u_i(\mathbf{x})$ to the fractional volume change, $\Delta v(\mathbf{y})$, within the reservoir

$$u_i(\mathbf{x}) = \int_V G_i(\mathbf{x},\mathbf{y})\Delta v(\mathbf{y})d\mathbf{y} \qquad (4)$$

where V is the reservoir volume (Rucci et al. 2013). The Green's function $G_i(\mathbf{x},\mathbf{y})$, depends upon the elastic properties of the overburden and the effort required for its computation depends upon the complexity of this elastic model. There are analytic (Okada 1992) and semi-analytic techniques (Wang et al. 2003) for homogeneous half-space and layered models, respectively, and semi-analytic successive approximations (Barbot et al. 2009), finite-difference and finite-element methods may be applied to fully three-dimensional models. The forward problem entails computing the displacements in the overburden given a distribution of volume change within the reservoir.

The inverse problem consists of using observations of overburden deformation to estimate volume change within the reservoir. This is a much more difficult task than the forward problem because of the loss of resolution with depth, due to the smoothing effects of the Green's function in equation (4). For example, in Figure 13 we show the impulse response of a point volume change at the reservoir level. That is, we impose a unit volume change in a single grid block of the reservoir and calculate

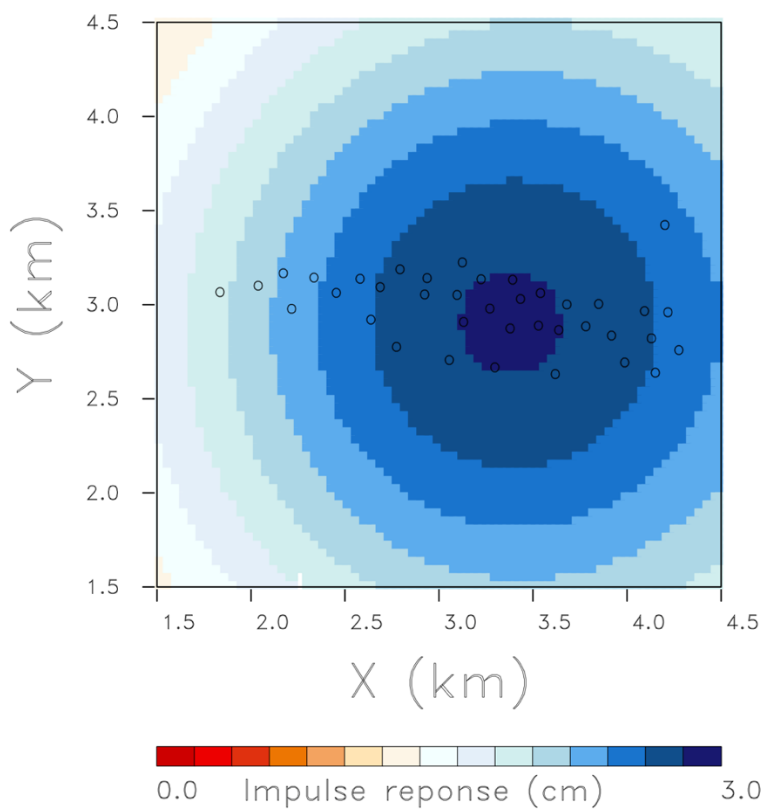

Figure 13. Impulse response due to a single grid block in the reservoir undergoing volume change.

the resulting line-of-sight displacement on the surface. Due to the roughly 3 km depth of the reservoir, the volume change in a compact grid block spreads to an equivalent surface anomaly of over 3 km in diameter. This smoothing effect, along with any errors and contamination due to other factors, such as the imperfect removal of atmospheric effects in the InSAR range change data, make the inverse problem unstable.

However, a stabilized inversion of the deformation can still be formulated, as a least squares minimization problem, and one can take advantage of the linearity of equation (4) in solving for the spatial distribution of the reservoir volume change (Vasco et al. 2017). That is, we can relate the InSAR range change, $r(\mathbf{x}_j, t)$, at a location $\mathbf{x}_j$ on the Earth's surface to the volume changes on N rectangular grid blocks distributed over the reservoir volume:

$$r(\mathbf{x}_j, t) = \sum_{n=1}^{N} R_n(\mathbf{x}_j) a_n(t) = \mathbf{R}(\mathbf{x}_j) \cdot \mathbf{v}(t) \quad (5)$$

where $R_n(x_j)$ is the integral of the projection of the Green's functions of the three displacement components along the look vector, $\mathbf{l}$, taken over the n-th grid block, P_n:

$$R_n(\mathbf{x}_j) = \int_{P_n} l_i \cdot G_i(\mathbf{x}_j, y) dV \quad (6)$$

Given a set of range change measurements we can write the associated collection of linear constraints as a large system of equations for the reservoir volume changes. The inverse problem entails solving this linear system for the volume changes during each time interval. This is accomplished using a least squares approach where we minimize the sum of the squares of the residuals.

Due to the difficulty of the inverse problem, it is important to devise appropriate regularization schemes to stabilize the process of estimating a solution. One particularly useful approach for volume changes that are induced by fluid extraction and injection into a reservoir, is a regularization or penalty term that favors volume changes near known well locations (Vasco et al. 2010, Rucci et al. 2013, Vasco et al. 2019). Such a penalty term utilizes the fact that the effective pressure changes surrounding the well are driving the volume changes within the reservoir. Conventional regularization terms, such as model norm and roughness penalty functions tend to produce excessively smooth solutions, exacerbating the loss of resolution with depth. Another way to regularize the inverse problem is via a model parameterization that accounts for known aspects of the source. For example, if the fluid volume changes are restricted to a specific formation with known boundaries one can incorporate that fact by restricting the source volume to that region. That is the case at Honor Rancho during normal operations, when the volume changes associated with the fluid injection and production are restricted to the relatively thin reservoir region shown in Figure 12.

In order to stabilize the inverse problem at Honor Rancho, we introduce a term which penalizes volume changes that are far from known well locations. This penalty function is based upon the hypothesis that the reservoir volume changes are primarily driven by fluid pressure and temperature changes due to injection and that these changes are largest near the well itself (Vasco et al. 2019). Therefore, we minimize the composite quadratic function in the volume changes $\mathbf{v}(t)$,

$$Q(\mathbf{v}) = (\mathbf{d} - \mathbf{M}\mathbf{v})^t \cdot (\mathbf{d} - \mathbf{M}\mathbf{v}) + \mathbf{v}^{\mathbf{t}}\mathbf{D}\mathbf{v} \tag{7}$$

where $\mathbf{d}$ is the vector of observed range changes, the data, $\mathbf{M}$ is a matrix with the j-th row given by $\mathbf{R}(\mathbf{x}_j)$, and a penalty matrix $\mathbf{D}$, that takes on larger values for cells that are farther from the injection

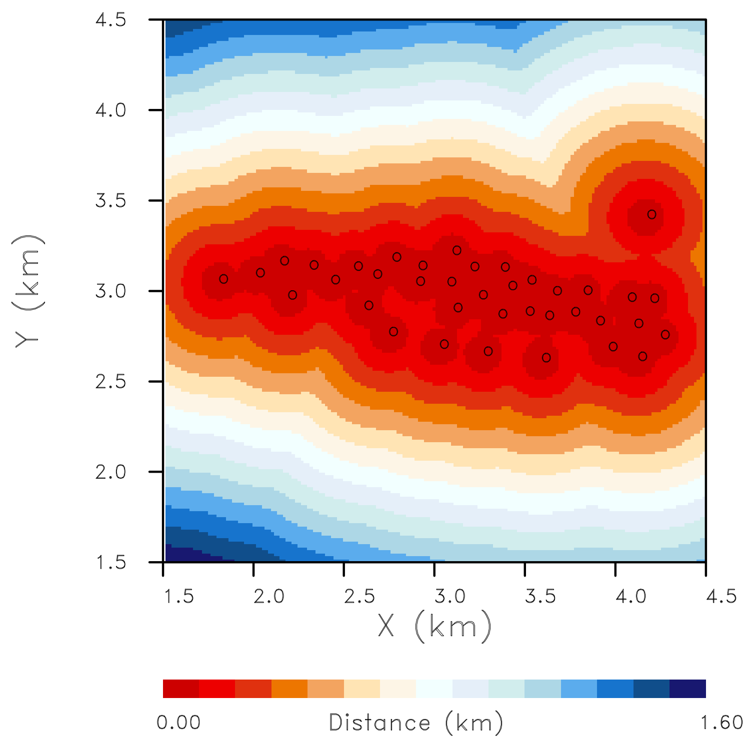

Figure 14. Distance penalty function that increases with distance to the nearest well. Such a function favors solutions that contain volume change near the well intersections with the reservoir. The intersection points are denoted by the open circles.

wells, as shown in Figure 14. While a heterogeneous distribution of elastic properties might distort the displacement field and result in greater deformation offset from the wells, such distortions should be accounted for in the fully three-dimensional elastic model used in the forward and inverse modeling. This type of penalty function has proven useful in other contexts. In particular, it has improved estimates of the distribution of groundwater usage in California's Central Valley by tying the aquifer volume changes to well locations and density (Vasco et al. 2019). If the injected and produced volumes are known, then the penalty term can be modified to try and match some fraction of the volume change around each well. This approach was used to obtain higher resolution estimates of overburden stress change above a producing oil field (Vasco et al. 2017).

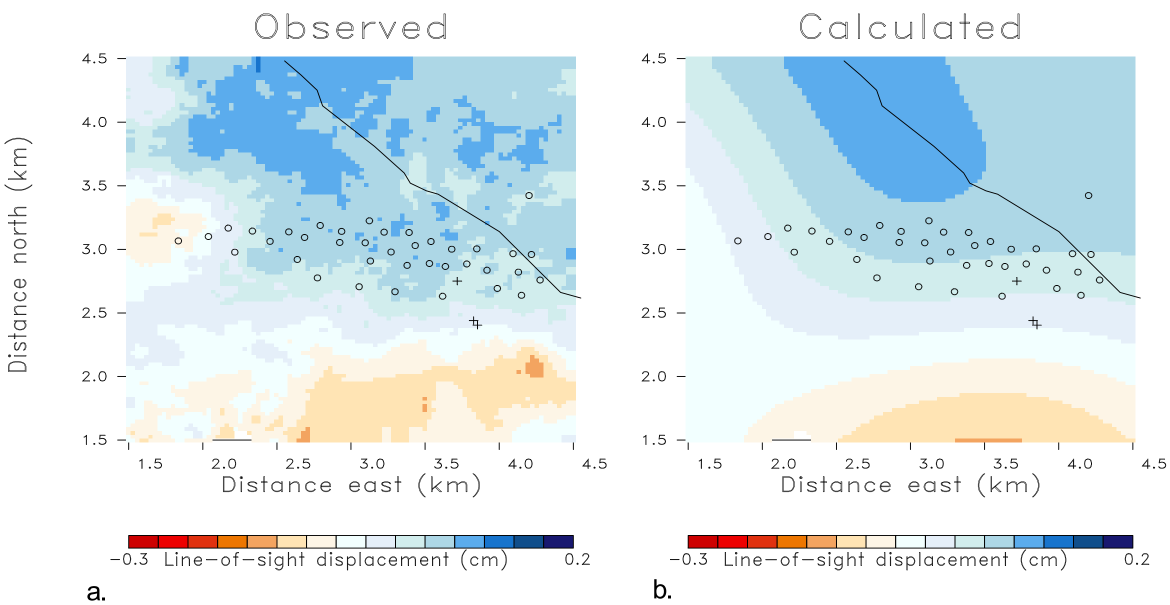

Figure 15. Observed (a.) and calculated (b.) line-of-sight displacement that occurred between May 29, 2016 and June 23, 2016. The open circles denote the bottom of the wells that are active in the gas field and the +'s denote shallower water injection wells. The solid line indicates the surface trace of the San Gabriel fault

The necessary equations for the minimum of the quadratic function $Q(\mathbf{v})$, with respect to the components of the volume change vector $\mathbf{v}$, produces the desired linear system of equations. As an example of this approach, consider the range change that occurred between May 29th and June 23rd in 2016 shown in Figure 15. The inferred displacements around the gas storage facility are generally 0.5 cm or less and are largest outside of the gas storage facility.

There are several reasons for deformation in the areas adjacent to the Honor Rancho gas storage facility. The storage site itself is situated on stable and competent bedrock of the Saugus formation which may limit or deflect the deformation laterally. Furthermore, the geological complexity of the area, with significant formation dip and a structural basin, as show in Figures 11 and 12, may contribute to the deflection of the peak deformation away from the center of the gas field. As is evident in Figure 3, the Way Side Canyon, Tapia, and Honor Rancho oil fields lie to the north of the gas storage facility and may be the source of the larger deformation visible in Figure 15. The region to the south of the site contains an alluvial drainage basin that is subject to seasonal changes. There is also an alluvial valley at the eastern edge of the group of wells that may also be strongly influenced by shallow hydrological changes. In addition, there are at least three documented faults, the Honor Rancho Thrust Fault, the Honor Rancho Normal Fault, and the F-1 Reverse Fault, cutting through the gas storage facility and these may extend to shallow depths. These three faults are roughly east-west trending. The seismicity plotted in the figure indicates that the area is tectonically active and several sequences of events trend in a northwesterly direction, sub-parallel to the San Gabriel fault zone which lies to the north of the field. The largest concentration of events lies at the southern edge of the region plotted in Figure 15 and appear to line up in east-west and northwesterly directions. These events may be associated with other faults, such as the Holser fault and adjacent sub-parallel faults, situated just to the south of the site (see Figure 1).

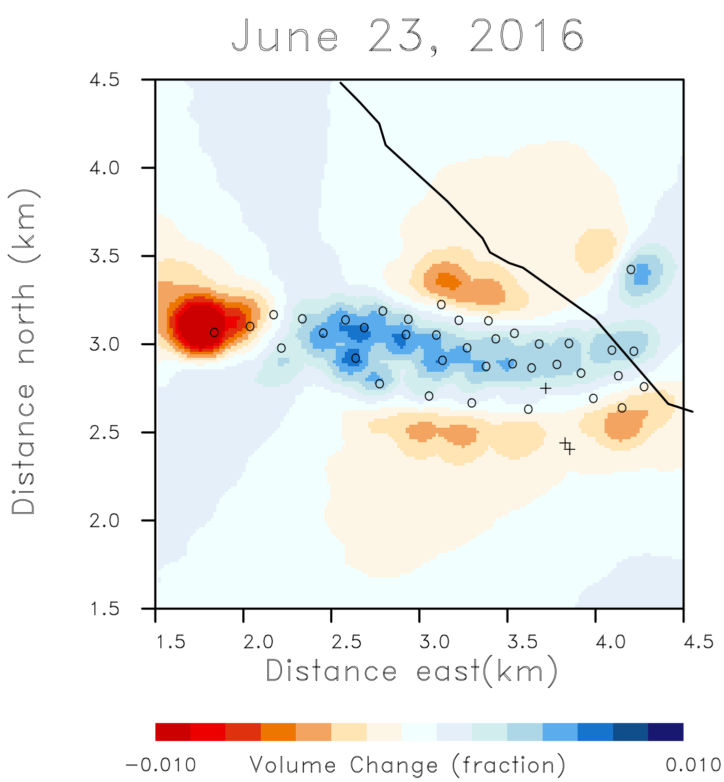

Figure 16. Fractional volume change obtained by an inversion of the line-of-sight displacement data. Blue hues signify volume increases while red denoted volume decreases.

Minimizing the penalized misfit (7) we can estimate the volume change in the reservoir that best explains the observed range change at the surface. The resulting estimate of volume change in the reservoir is shown in Figure 16. The solution in Figure 16 provides a model of volume change within the reservoir that best explains the observed displacements between May 29th and June 23rd, 2016. The model generally contains fractional volume increases at and around the injection wells, as would be expected in the month of June when gas in injected into the reservoir for use in the coming winter. There are volume decreases to the north, south, and west of the gas storage site that might be due to stress transfer from the area of injection. That is, the stress changes due to volume increases and fracture aperture changes in an elastic or poroelastic medium can induce complicated stress changes in the surrounding region (Segall 1989, Lambert and Tsai 2020, Kettlety et al. 2020) that can produce associated volume changes. These effects have been observed in experiments involving fluid withdrawal from a sub-horizontal fracture zone, in both estimated fracture volume change and in borehole pressure measurements (Karasaki et al. 2000, Vasco et al. 2001). The effect can be amplified by geologic heterogeneity mentioned above, that can concentrate the stress changes and increase them by an order of magnitude (Johnson and Majer 2017). Unfortunately, it is not possible to compare the volume changes around the well with injection and production data because the only measurements are co-mingled volumes from all of the wells and the individual well rates are not

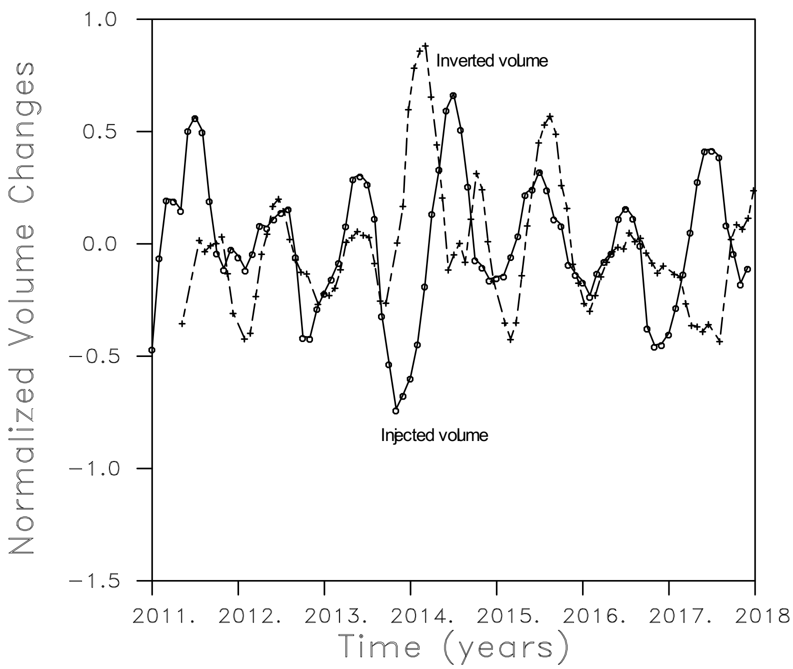

Figure 17. (Solid line) Monthly injected gas volume (normalized) obtained by summing over all of the wells operating in the storage facility at Honor Rancho. (Dashed line) Total monthly volume changes (normalized) obtained from the inverted models after summing over all grid blocks in the area of the gas storage reservoir.

measured and must be inferred. Because factors such as atmospheric variations, tectonic strain, and adjacent deformation from nearby oil fields and hydrological variations can also produce smooth variations of the same magnitude and scale as the reservoir, at this point it is important not to over-interpret the estimated reservoir volume changes presented in Figure 16.

We conducted inversions for all of the available InSAR observation intervals between 2011 and 2018 in order to image the volume changes within the reservoir as a function of time. Thus, we obtain 92 snapshots of reservoir volume change obtained at intervals of roughly 24 days. From these snapshots we can sum over the volume changes in all of the grid blocks in our model in order to estimate the total volume change during each time interval, as plotted in Figure 17. One observes generally periodic behavior in the estimated reservoir volume changes, with the volume increasing in the late winter and early spring, leading to a peak in the summer, followed by a decrease in the fall and early winter. Note that this is the opposite effect that one would expect from seasonal rainfall which would generate uplift in the winter and subsidence in the summer. The largest volume changes occurred in 2014 and the increase in volume appears to have started earlier, in late 2013, than it does in most other years. It is worthwhile comparing the estimated reservoir volume changes with the volume of natural gas injected into the reservoir during the same time period. It is difficult to relate the inverted changes, which represent the total grid block volume changes within the reservoir, with the injected gas volumes in a quantitative sense. A quantitative comparison requires a complete understanding of the poroelastic behavior of the reservoir in order to map injected fluid volumes to the resulting total rock volume change. At this point we do not have the necessary reservoir properties that are needed for such a mapping. Therefore, in Figure 17 we compared the normalized estimated volume changes with the normalized total injected/produced volumes.

In general, a quasi-periodic behavior is evident in Figure 17, with the reservoir volume increasing in the late winter and early spring, and decreasing in the fall and early winter. As in the inversion results, the largest volume increase occurs in 2014. Note that while there is fairly good agreement with the temporal change in 2012, 2013, 2015, and 2016, in other years the inverted volume changes differ significantly from the injected volumes. For example, in 2014 there is a double peak in the inverted volumes while there is a single peak in the measured injected gas volume and the temporal variation looks quite different. Furthermore, there is a large difference between the inverted total volume and the injection volume in 2017, the year of the large and sustained rainfall and river discharge (Figure 9). We will have more to say about the discrepancy in 2014 below.

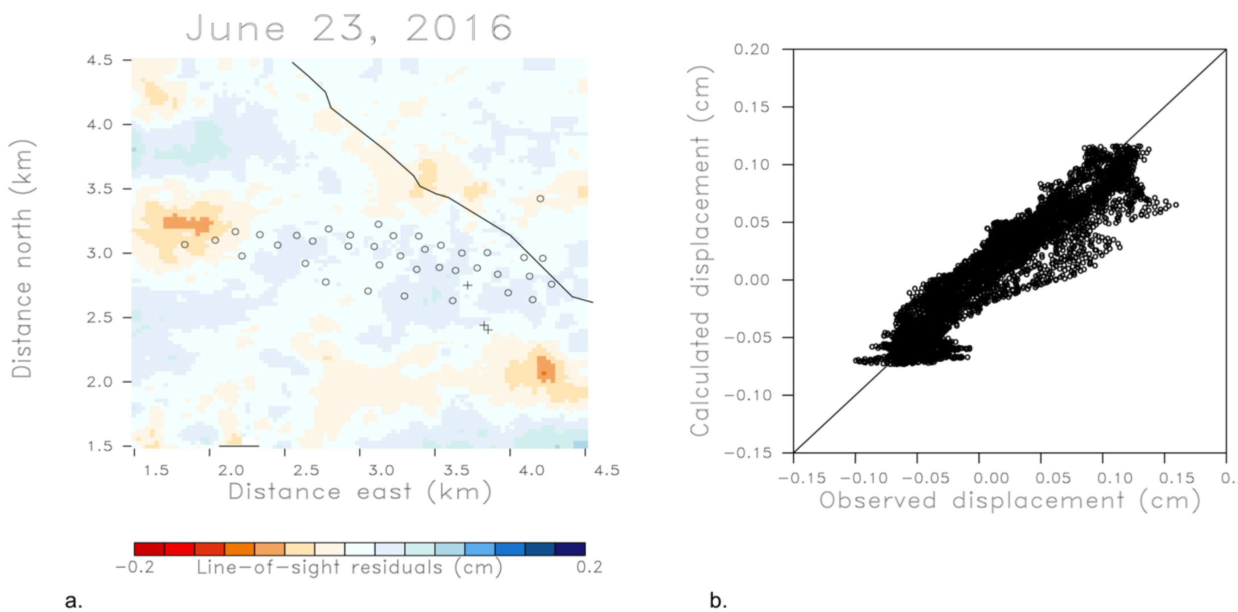

Figure 18. (a.) Residual pattern plotted on a map. (b.) Observed versus calculated displacements.

We can use the estimates of reservoir volume change and the observed range changes to identify anomalous events, that is time intervals during which it is difficult or impossible to fit the observed range changes with volume changes solely within the reservoir. The basic idea is to invert the InSAR observations for volume change in the reservoir, as above, and then consider the residuals, the misfit to the observations. We can plot the sum of the misfits for each InSAR observation over the gas storage site to generate a total misfit for the area of interest. By examining the variation of these total misfits in time we can estimate the overall root-mean-squared misfit that is typically achieved for each inversion. This provides an estimate of the noise level in our data. As noted above, the noise level can include range change due to factors such as shallow hydrologic changes and atmospheric variations as well as random errors.

In order to determine the temporal variation in residuals, and to define normal and anomalous ground movement, we followed the procedure described above for removing the possible reservoir signal and calculating line-of-sight residuals. The area over which the residuals were computed, shown in Figure 18, encompasses land surface somewhat to the north and south of the gas storage facility. Residuals were computed for the 93 intervals, from May 5, 2011 to January 20, 2018. The root-mean-squared (RMS) residual variations are plotted in Figure 19 as a function of time. From the time series we observe a natural background residual amplitude of around 2-3 mm with generally higher residuals in 2011/2012 and late 2016 and in 2017. In addition, there are two anomalous events in 2014 when the residuals approach or exceed 6 mm. These unusually large residuals warrant further investigation, particularly the episodes in 2014. We can gain some insight into the source of these large-amplitude events if we examine the individual residuals plotted in map view.

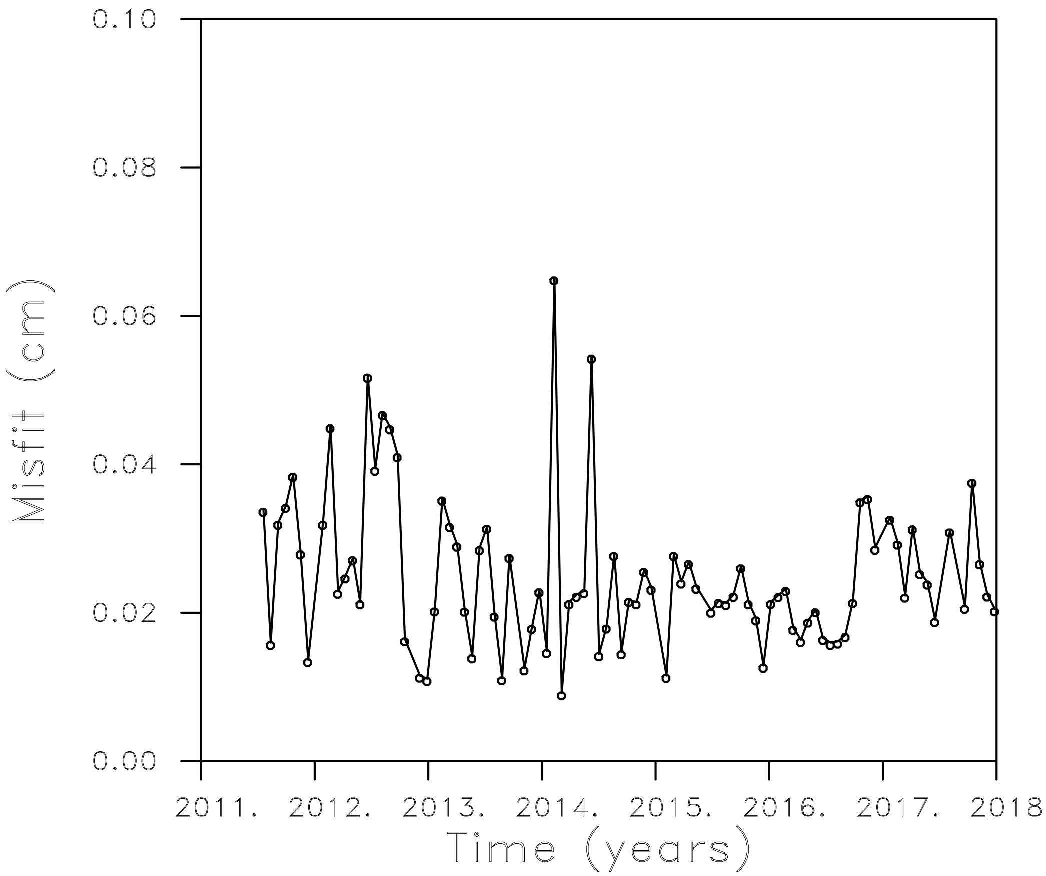

Figure 19. Temporal variation in the root-mean-squared residual amplitudes. Each point in this plot represents the total misfit over the gas storage field, such as that plotted in the right panel of Figure 18. The RMS misfit is small due to the presence of many small values which lowers the calculated mean value. The variation between 0.2 and 0.3 cm, also agrees with the scatter about the best-fit line in Figure 18.

First, consider the residual distribution in July 2011 (Figure 20) for the region around the gas storage facility. There are large residuals to the south of the storage site and a striking change in the sign in the line-of-sight displacement (Figure 20). The rapid spatial variation would seem to indicate a shallow source for the anomaly. The orientation, which is sub-parallel to the San Gabriel Fault and linear trends in seismicity, suggests some form of structural control on the process producing the largest residuals. Possible sources of this inferred deformation signal include shallow hydrological variations or local shallow fault creep transients, but they could also represent atmospheric noise. The Holser fault is located in this area (Yeats et al. 1994, Yeats and Stitt 2003) and is thought to have

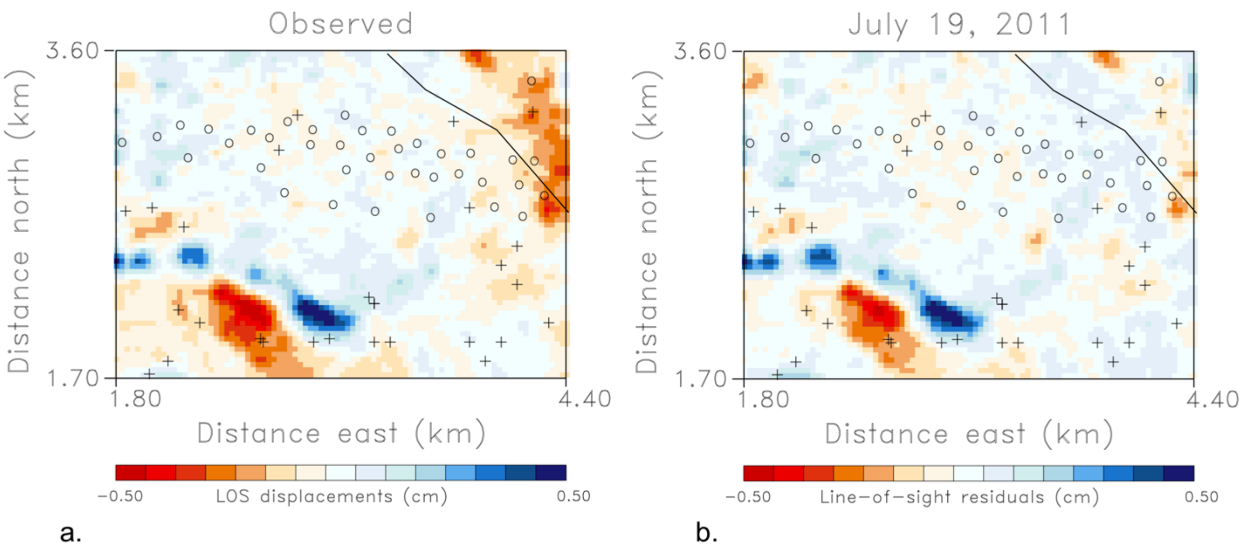

Figure 20. (a.) Line-of-sight displacements for the time interval ending on July 19, 2011. (b.) Line-of-sight residuals associated with InSAR data gathered in June and July of 2011. The residuals were obtained by subtracting the calculated displacements produced by the reservoir volume changes. The +'s denote historical earthquakes that have occurred since 1931.

a small but significant slip rate of 1.7 mm/year (Marshall et al. 2013). The amplitude of the changes observed in Figure 20, over 5 mm, exceeds the estimated errors of the InSAR measurements. The largest residuals are in the alluvial valley to the south of the natural gas storage facility and are unlikely to be related to its operation.

Next, we consider the two large amplitude events in 2014 that are about three times the RMS misfit of the normal background variations (Figure 19). The spatial distribution of residuals associated with the events are plotted in Figure 21. The residuals associated with the first event around March 4, 2014 contains a rapid change from positive to negative line-of-sight displacement over the west central portion of the gas storage field, similar in structure to the feature found previously to the south of the field. In fact, there is also a similar pattern of deformation in the southern area as seen in Figure 20 but of opposite polarity. The deformation over the gas storage facility is significant because it occurs in the more competent Saugus formation and not in highly porous alluvium which may not be subject to strong hydrological variations. However, there are incised valleys from the east and west that are south and sub-parallel to the San Gabriel fault that may indicate a fault and associated heterogeneity below these anomalies. The area above the gas storage site is a topographic high that is not likely to accumulate significant groundwater, and a stress change is a possible source of the observed displacements. In fact, the field operators confirmed that the gas pressure in the field was reduced to particularly low values during this time, as indicated by the peak withdrawal at the

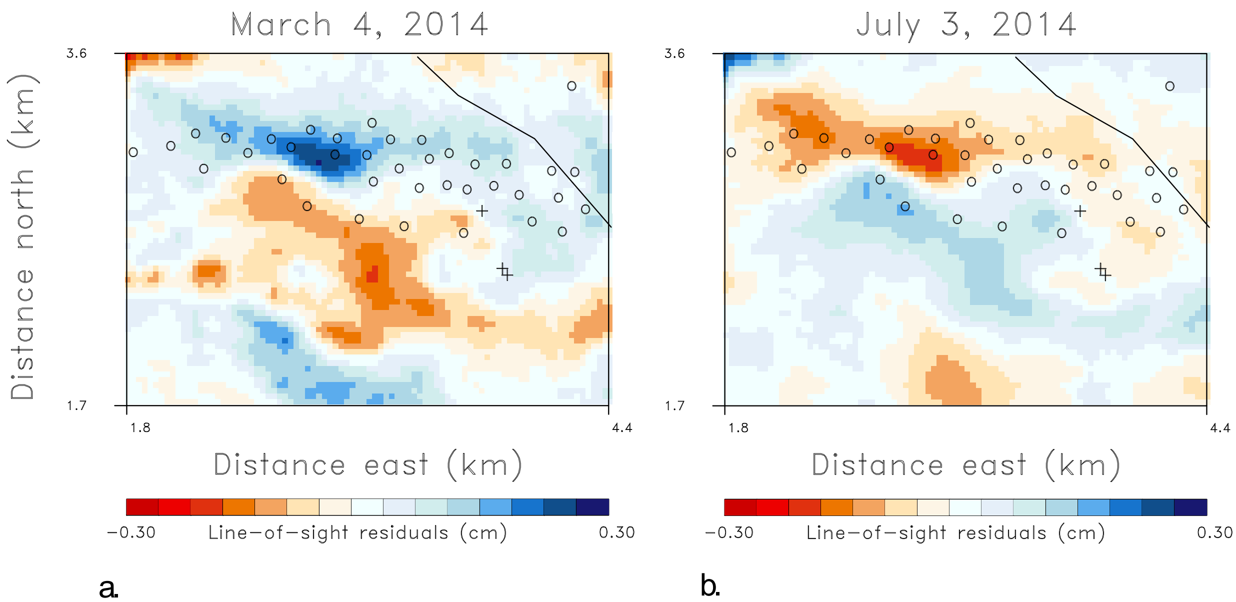

Figure 21. (a.) Residual spatial distribution for the anomalous event around March 4, 2014. (b.) Spatial distribution of the residuals corresponding to the anomalous event around July 3, 2014. The open circles denote wells from the gas storage facility while the +'s denote water injection wells.

end of 2013 (Figure 17), possibly leading to large effective stress changes in the reservoir. This first large anomaly in Figure 21 is followed by a slightly lower-value residual peak, corresponding to deformation around July 3, 2014. We also plot the spatial distribution of residuals for this event in Figure 21b. The largest anomalies are in the same locations as those in the March 4th event but they are opposite in sign, signifying movement away from the satellite to the north and towards the satellite to the south. In the summer months the Honor Rancho gas field is undergoing replenishment and an increase in reservoir pressure, the opposite of the winter withdrawals. It is interesting that the two anomalous events coincide with the disruption of the 2014 peak in volume change plotted in the right panel of Figure 17, further evidence of unusual behavior in that time interval.

A shallow hydrological source is still a possibility and an alternative explanation of the anomalies in 2014 because there are groundwater variations in the area, including several shallower water wells

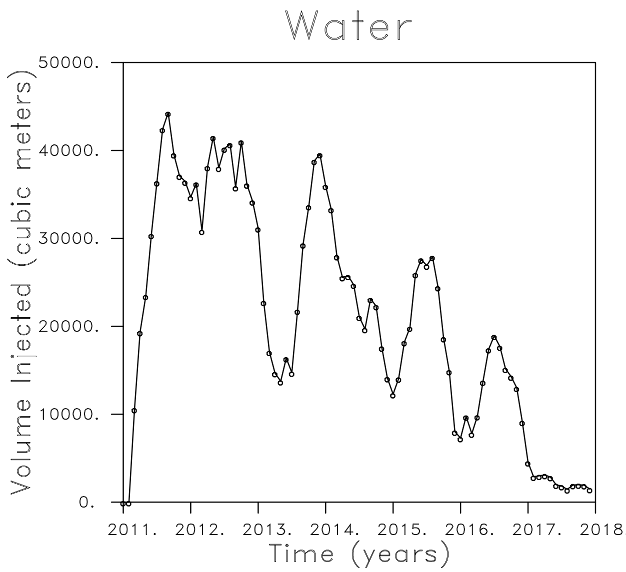

Figure 22. Volume of injected water during the monitoring period.

as shown by the +'s in Figure 21. Two of the water wells might lie along a southeast extension of the line separating the positive and negative anomalies in Figure 21 and, as indicated below, possibly intersecting a permeable pathway. The volume of injected water was significant during the years prior to the anomalous events in 2014 (Figure 22). Large temporal variations in rainfall and stream discharge are also evident in Figure 10. As noted above, interactions between a fault system and aquifers can lead to abrupt changes in ground displacement (Schmidt and Burgmann 2003). We have already seen how the sustained heavy rains in late 2016 and early 2017 are a likely cause for significant uplift to the west of the gas storage facility (see Figures 6 and 8).

Hydrological factors could also produce the large increase in residuals between 2016 and 2017 in the residual time series plotted in Figure 19. The rain leads to changes in the shallow aquifers over and around the gas storage facility leading to generally larger residuals, though the level of misfit is roughly half the magnitude of the earlier residuals in 2012 and for the two events in 2014. A plot of the spatial distribution of residuals associated with March 12, 2017 reveals a bimodal pattern of slightly higher residuals, to the south of the natural gas storage field, similar to the one that was observed in 2011, as plotted in Figure 23.

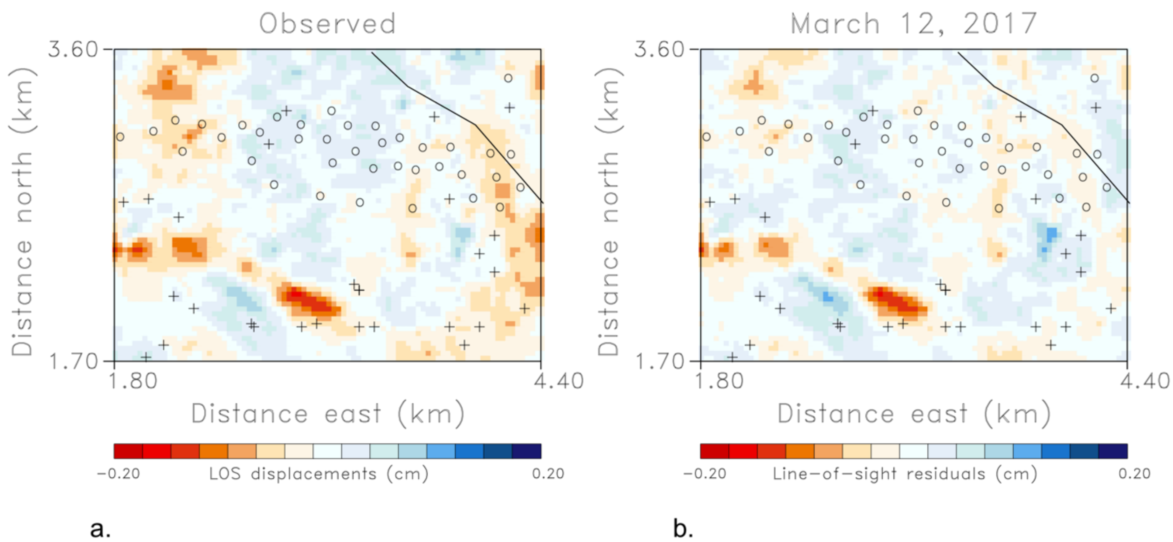

Figure 23. (a.) Observed line-of-sight displacements around March 12, 2017. (b) Residuals for displacements around March 12, 2017. The +'s denote historical earthquakes that have occurred since 1931.

Discussion and Conclusions

Interferometric Synthetic Aperture Radar observations provide a cost-effective method for monitoring an operating gas storage facility, even one as deep as the Honor Rancho field which lies roughly 3 kilometers below the surface of the Earth. While the surface deformation attributable to activities within the reservoir is small and can be accounted for through inversions for reservoir volume changes, processes above and away from the reservoir, such as hydrological deformation, slip on shallow faults, leaks from wells above the reservoir, and landslides lead to larger signals that can be identified through their sizable residuals in a given observation interval. Two events in 2014 in the InSAR data from Honor Rancho indicates unusual patterns of surface deformation that warrant further investigation. The greatest line-of-sight displacements for these two events are along a valley that cuts across the Honor Rancho facility. The valley may signify a tectonic feature, such as a fault. At the very least, it suggests that hydrological factors may be important in the immediate area. Known activities, such as shallow water injection, need to be accounted for in order to improve the monitoring reliability and to reduce the possible misinterpretation of larger InSAR residuals. Anomalous events only signify a time interval where the residuals should be examined and interpreted. Because the reservoir signal is removed in the inversion, anomalous events are unlikely to signify an event within the confines of the gas storage facility or within the reservoir itself. Rather, there are more likely to be caused by processes above the reservoir which produce surface deformation of a different character than that produced by the reservoir.

It is unclear what caused the well-resolved ground uplift to the west of the gas storage facility as discussed above and plotted in Figure 8. Given that the spatial pattern of this deformation feature does not clearly correlate with the well distribution at the storage facility, we conclude that this deformation feature is unlikely caused by processes associated with the storage operations. Our leading hypothesis is that the uplift to the west of the wells is associated with the higher-than-average precipitation in early 2017. Particularly, the intensive rainfall starting from February, 2017 quickly rose up the water level in the Castaic Lake, which is only a few kilometers upstream and north of the Honor Rancho gas storage facility. It is possible that the surface uplift (Figure 8) is a result of elastic response of the porous Earth's crust to a rapid recharge following the intensive rainfall. We note, however, that this uplift feature has not subsided in the subsequent years, and further analysis is needed in order to resolve the source of the observed deformation. An ongoing study of InSAR subsidence and rebound in the Central Valley, to the northeast, has produced well level data that indicates that the water table rose substantially in 2017 in response to the same wet winter rains, and remained at this elevated level through at least the end of 2019. The well level variations are very similar to the variations in line-of-sight displacements in Figure 7, so a long-lasting elevation of the water table is not out of the question.

The residual patterns that we have examined indicate instances of bi-modal displacements of opposite sign, as seen in Figures 20, 21, and 23. These rapid spatial variations suggest shallow sources for the deformation, such as near surface hydrological changes. Upon detecting these patterns in the residuals, we searched the line-of-sight displacement data for evidence of similar bimodal patterns in the southern edge of our study area. In addition to the event of March 12, 2017, we found two other patterns in the raw data. The bi-modal patterns are in the same location south of the Honor Rancho storage facility and have the same orientation and extent as the residual patterns. The amplitude of the displacements is generally of the order of a few milli-meters, similar in magnitude or smaller than the deformation in the surrounding region. As noted above, the orientation of the features parallels the San Gabriel fault and the Holser fault (Yeats et al. 1994, Yeats and Stitt 2003).

The procedure for identifying anomalous events discussed in this paper is general and applicable to natural events and industrial operation involving the injection and/or withdrawal of fluids into/from the Earth. In fact, an early version of this approach was implemented in an active oil field (Vasco et al. 2017). InSAR monitoring has also identified anomalous behavior associated with the large-scale geological storage of carbon dioxide (Vasco et al. 2010), though no formal monitoring workflow for event detection was ever developed in that study. The procedure could also be used, in conjunction with earthquake detection, for natural events such as monitoring volcanic activity and the improved understanding of impending eruptions.

Acknowledgments

This work was supported by the California Energy Commission (CEC) and by Lawrence Berkeley National Laboratory (LBNL) under Department of Energy Contract No. DE-AC02-05CH11231. We would like to thank our project partner Southern California Gas Company, especially Daniel Shapiro for collaboration and data sharing; the CEC program manager Yahui Yang for constructive comments.

Data Availability

The data underlying this article will be shared upon request to the corresponding author.

REFERENCES

Barbot, S., Fialko, Y., and Sandwell, D., 2009. Three-dimensional models of elastostatic deformation in heterogeneous media, with applications to the Eastern California Shear Zone, *Geophysical Journal International*, **179**, 500-520.

Benetatos, C., Codegone, G., Ferraro, C., Mantegazzi, A., Rocca, V., Tango, G., and Trillo, F., 2020. Multidisciplinary analysis of ground movements: An underground gas storage case study, *Remote Sensing*, **12**, 3487, doi:10.3390/rs12213487.

Berardino, P., Fornaro, G., Lanari, R., 2002. A new algorithm for surface deformation monitoring based on small baseline differential SAR interferograms. *IEEE transactions on Geoscience and Remote Sensing,* **40** (11), 2375-2383.

Bürgmann, R., P. A. Rosen, and E. J. Fielding 2000. Synthetic aperture radar interferometry to measure Earth's surface topography and its deformation, *Annu. Rev. Earth Planet. Sci.*, **28**, 169-209.

Carannante, S., E. D'Alema, P. Augliera, and G. Franceschina 2020. Improvement of microseismic monitoring at the gas storage concession "Minerbio Stoccaggio" (Bologna, Northern Italy), *Journal of Seismology*, **24**, 967-977.

Carnec, C., and H. Fabriol, 1999. Monitoring and modeling land subsidence at Cerro Prieto geothermal field, Baja California, Mexico, using SAR interferometry, *Geophys. Res. Lett.,* **26**, 1211-1214

Cesca, S., D. Stich, F. Grigoli, A. Vuan, J. A. Lopez-Comino, P. Niemz, E. Blanch, T. Dahm, and W. L. Ellsworth, 2021. Seismicity at the Castor gas reservoir driven by pore pressure diffusion and asperities loading, *Nature Communications*, **12**:4783, 1-13, doi.org/10.1038/s41467-021-24949-1.

Chaussard, E., P. Milillo, R. Bürgmann, D. Perissin, F. E.J., and B. Baker, 2017. Remote sensing of ground deformation for monitoring groundwater management practices: application to the Santa Clara Valley during the 2012-2015 California drought, *J. Geophys. Res. Solid Earth*, *122*(10), 8566–8582, doi:10.1002/2017JB014676.

Conley, S., G. Franco, I. Faloona, D. R. Blake, J. Peischl, and T. B. Ryerson, 2016. Methane emissions from the 2015 Aliso Canyon blowout in Los Angeles, CA. *Science,* **351**, 6279, pp. 1317-1320. DOI: 10.1126/science.aaf2348

Evans, D.J., 2009. A review of underground fuel storage events and putting risk into perspective with other areas of the energy supply chain, in Underground Gas Storage, Worldwide Experiences and Future Development in the UK and Europe, The Geological Society, London, Special Publications, 313, pp.173–216.

Ferretti, A., Prati, C. and Rocca, F. 2001. Permanent Scatterers in SAR Interferometry, *IEEE Transactions on Geoscience and Remote Sensing*, **39**(1), 8 -20.

Ferretti, A., A. Fumagalli, F. Novali, C. Prati, F. Rocca, and A. Rucci 2011. A new algorithm for processing interferometric data-stacks: SqueeSAR, *IEEE Trans. Geosci. Remote Sens.*, **49**(9), doi: 10.1109/TGRS.2011.2124465.

Ferretti, A. 2014. *Satellite InSAR Data – Reservoir Monitoring from Space*. EAGE Publications.

Fielding, E. J., Blom, R. G., and Goldstein, R. M. 1998. Rapid subsidence over oil fields measured by SAR interferometry, *Geophysical Research Letters*, **25**, 3215-3218.

Haghighi, M. H., and Motagh, M., 2017. Sentinel-1 InSAR over Germany: Large-scale interferometry, atmospheric effects, and ground deformation mapping, *zfv*, **142**, 245-256, doi 10.12902/zfv-0174-2017.

Hetz, G., Datta-Gupta, A., Przybysz-Jarnut, J. K., Lopez, J. L., and Vasco, D. W. 2020. Using onset times from frequent seismic surveys to understand fluid flow at the Peace River Field, Canada, *Geophysical Journal International*, **223**, 1610-1629.

Hooper, A. 2008. A multi-temporal InSAR method incorporating both persistent scatterer and small baseline approaches, *Geophysical Research Letters***, 35**, L16302, 1-5.

Hooper, A., D. Bekaert, K. Spaans, M. Arikan, 2012, Recent advances in SAR interferometry time series analysis for measuring crustal deformation, Tectonophysics, 514-517, pp.1-13, doi:10.1016/j.tecto.2011.10.013

Hooper, A., H. Zebker, P. Segall, and B. Kampes 2004, A new method for measuring deformation on volcanoes and other natural terrains using InSAR persistent scatterers, *Geophys. Res. Lett.*, ***31***, doi:10.1029/2004GL021737.

Hooper, A. 2008. A multi-temporal InSAR method incorporating both persistent scatterrer and small baseline approaches, *Geophys. Res. Lett.*, *35*(L16302), doi:10.1029/2008GL03465.

Houlié, N., G. Funning, and R. Bürgmann 2016. Use of a GPS-derived troposphere model to improve InSAR deformation estimates in the San Gabriel Valley, California, *IEEE Transactions on Geoscience and Remote Sensing*, ***9***(99), 5365-5374, doi:10.1109/TGRS.2016.2561971.

Jeanne, P., Zhang Y., and Rutqvist J. 2020. Influence of hysteretic stress path behavior on seal integrity during gas storage operation in a depleted reservoir, *Journal of Rock Mechanics and Geotechnical Engineering*, https://doi.org/10.1016/j.jrmge.2020.06.002.

Jha, B., Bottazzi, F., Wojcik, R., Coccia, M., Bechor, N., McLaughlin, D., Herring, T., Hager, B. H., Mantica, S., and Jaunes, R., 2015. Reservoir characterization in an underground gas storage field using joint inversion of flow and geodetic data, *International Journal for Numerical and Analytical Methods in Geomechanics*, **39**, 1619-1638.

Jiang, G., Qiao, X., Wang, X., Lu, R., Liu, L., Yang, H., Su, Y., Song, L., Wang, B., and Wong, T.-F., 2020. GPS observed horizontal ground extension at the Hutubi (China) underground gas storage facility and its applications to geomechanical modeling for induced seismicity, *Earth and Planetary Science Letters*, **530**, 1-12.

Johnson, L. R., and Majer, E. L., 2017. Induced and triggered earthquakes at The Geysers geothermal reservoir, *Geophysical Journal International,* **209**, 1221-1238.

Karasaki, K., Freifield, B., Cohen, A., Grossenbacher, K., Cook, P., and Vasco, D., 2000. A multidisciplinary fractured rock characterization study at Raymond field site, Raymond, Ca, *Journal of Hydrology*, **236**, 17-34.

Kettlety, T., Verdon, J. P., Werner, M. J., and Kendall, J. M., 2020. Stress transfer from opening hydraulic fractures controls the distribution of induced seismicity, *Journal of Geophysical Research*, **125**, 1-21.

King, N. E. et al., 2007. Space geodetic observation of expansion of the San Gabriel Valley, California, aquifer system, during heavy rainfall in winter 2004–2005, J. Geophys. Res., **112**, B3, Art. no. B03409.

Lambert, V., and Tsai, V. C., 2020. Time-dependent stresses from fluid extraction and diffusion with applications to induced seismicity, *Journal of Applied Mechanics*, **87**, 1-13.

Lanari, R., Mora, O., Manunta, M., Mallorqui, J. J., Berardino, P, and Sansosti, E. 2004. A small baseline approach for investigating deformations on full-resolution differential SAR interferograms, *IEEE Transactions on Geoscience and Remote Sensing*, **42**, 1377-1386.

Massonnet, D., T. Holzer, and H. Vadon 1997. Land subsidence caused by the East Mesa Geothermal Field, California, observed using SAR interferometry, *Geophys. Res. Lett.*, **24**(8), 901–904.

Marshall, S. T., Funning, G. J., and Owen, S. E. 2013. Fault slip rates and interseismic deformation in the western Transverse Ranges, California, *Journal of Geophysical Research*, **118**, 4511-4534.

Mayuga, M. N., and Allen, D. R. 1969. Subsidence in the Wilmington Oil Field, Long Beach, California, USA. *Tokyo Symposium on Land Subsidence*

MDA, 2013. *Playa del Rey, California InSAR Ground Deformation Monitoring Interim Report* H., Ref: RV-14524, MDA Spatial Services, Ontario, Canada

Ojha, C., Werth, S., & Shirzaei, M. 2019. Groundwater loss and aquifer system compaction in San Joaquin Valley during 2012–2015 drought. Journal of Geophysical Research: Solid Earth, 124, 3127–3143. https://doi.org/10.1029/2018JB016083

Okada, Y., 1992. Internal deformation due to shear and tensile faults in a half-space, *Bulletin of the Seismological Society of America*, **82**, 1018-1040.

Osmanoğlu, B., Sunar, F., Wdowinski, S., & Cabral-Cano, E. 2016. Time series analysis of InSAR data: Methods and trends. *ISPRS Journal of Photogrammetry and Remote Sensing*, *115*, 90–102. https://doi.org/10.1016/j.isprsjprs.2015.10.003

Poland, J. F., Lofgren, B. E., Ireland, R. L., & Pugh, R. G. 1975. Land subsidence in the San Joaquin Valley, California, as of 1972, U.S. Geol. Surv. Prof. Pap., 437-H, 77 pp.

Qiao, X., Q., Wei, C., Dijin, W., Zhaosheng, N., Zhengsong, C., Jie, L. Xiaoqiang, W., Yu, L., Tan, W., and Guangcai, F., 2018. Crustal deformation in the Hutubi underground gas storage site in China observed by GPS and InSAR measurements, *Seismological Research Letters*, **89,** 4, 1467-1477.

Rapant, P, Struhar, J., and Lazecky, M., 2020. Radar interferometry as a comprehensive tool for monitoring the fault activity in the vicinity of underground gas storage facilities, *Remote Sensing*, **12**, 271, doi:10.3390/rs12020271.

Rucci, A., Vasco, D. W. and Novali, F. 2013. Monitoring the geologic storage of carbon dioxide using multicomponent SAR interferometry. *Geophysical Journal International*, **193**(1), 197-208.

Rutqvist, J., 2011. Status of the TOUGH-FLAC simulator and recent applications related to coupled fluid flow and crustal deformations. *Comput*. *Geosci*. **37**, 739–750.

Samsonov, S., d'Oreye, N. 2012. Multidimensional time series analysis of ground deformation from multiple InSAR data sets applied to Virunga Volcanic Province. *Geophysical Journal International*, **191**, 1095-1108, http://dx.doi.org/10.1111/j.1365-246X.2012.05669.x.

Samsonov S., van der Koij M. and Tiampo, K., 2011. A simultaneous inversion for deformation rates and topographic errors of DInSAR data utilizing linear least square inversion technique, *Computers & Geosciences*, **37** (8), 1083-1091

Sandwell, D., Mellors, R., Tong, X., Wei, M., & Wessel, P. 2011. Open radar interferometry software for mapping surface deformation. Eos, Transactions American Geophysical Union, 92(28), 234. https://doi.org/10.1029/2011EO280002

Schmidt, D. A., and Burgmann, R., 2003. Time-dependent land uplift and subsidence in the Santa Clara valley, California, from a large interferometric synthetic aperture radar data set. Journal of Geophysical Research, **108**, 1-13.

Segall, P. 1989. Earthquakes triggered by fluid extraction, *Geology*, **17**, 942-946.

Shirazaei, M., Ellsworth, W. L., Tiampo, K. F., Gonzalez, P. J., and Manga, M. 2016. Surface uplift and time-dependent seismic hazard due to fluid injection in eastern Texas, *Science*, **353**, 1416-1419.

Teatini, P, Castelletto, N., Ferronato, M., Gambolati, G., Janna, C., Cairo, E, Marzorati, D., Colombo, D., Ferretti, A., Bagliani, A., and Bottazzi, F., 2011. Geomechanical response to seasonal gas storage in depleted reservoirs: A case study in the Po River basin, Italy, *Journal of Geophysical Research*, **116**, 1-21

Vasco, D. W., Karasaki, K., and Kishida, K., 2001. A coupled inversion of pressure and surface displacement, *Water Resources Research*, **37**, 3071-3089.

Vasco, D. W., Rucci, A., Ferretti, A., Novali, F., Bissell, R. C., Ringrose, P. S., Mathieson, A. S., and Wright, I. W., 2010. Satellite-based measurements of surface deformation reveal fluid flow associated with the geological storage of carbon dioxide, *Geophysical Research Letters*, **37**, L03303, 1-5, doi:10.1029/2009GL041544.

Vasco, D. W., Harness, P., Pride, S., and Hoversten, M. 2017. Estimating fluid-induced stress change from observed deformation, *Geophysical Journal International*, **208**, 1623-1642.

Vasco, D. W., Farr, T. G., Jeanne, P., Doughty, C., and Nico, P., 2019. Satellite-based monitoring of groundwater depletion in California's Central Valley, *Nature Scientific Reports*, **9**, 16043, doi.org/10.1038/s41598-019-52371-7.

Wang, K., & Fialko, Y., 2018. Observations and Modeling of Coseismic and Postseismic Deformation Due To the 2015 M w 7.8 Gorkha (Nepal) Earthquake. *Journal of Geophysical Research: Solid Earth*, ***123***(1), 761–779. https://doi.org/10.1002/2017jb014620

Wang, R., Martin, F., and Roth, F., 2003. Computation of deformation induced by earthquakes in a multi-layered elastic crust-Fortran programs EDGRN/EDCMP, *Comp. Geosci*., **29**, 195-207.

Yeats, R. S., Huftile, G. J., and Stitt, L. T. 1994. Late Cenozoic tectonics of the East Ventura Basin, Transverse Ranges, California, *AAPG Bulletin*, **78**, 1040-1074.

Yeats, R. S., and Stitt, L. T. 2003. Ridge Basin and San Gabriel faults in the Castaic Lowland, Southern California, *Geological Society of America Special Papers*, **367**, 131-156.

Xu, X., Sandwell, D. T., Tymofyeyeva, E., González-Ortega, A., & Tong, X. 2017. Tectonic and anthropogenic deformation at the Cerro Prieto geothermal step-over revealed by Sentinel-1A InSAR. *IEEE Transactions on Geoscience and Remote Sensing*, **55**(9), 5284–5292. https://doi.org/10.1109/TGRS.2017.2704593

Yang, Q., W. Zhao, T. H. Dixon, F. Amelung, W. S. Han, P. Li 2015. InSAR monitoring of ground deformation due to CO_2 injection at an Enhanced Oil Recovery Site, West Texas. *International Journal of Greenhouse Gas Control* **41**, 116-126, doi:10.1016/j.ijggc.2015.06.016

Zaman, M. M., Abdulraheem, A., and Roegiers, J. C. 1995. Chapter 8: Reservoir compaction and surface subsidence in the North Sea Ekofisk field, *Developments in Petroleum Science,Volume* , **41**, 373-423.

Zhou, P., H. Yang, B. Wang, and J. Zhuang 2019. Seismological investigations of induced earthquakes near the Hutubi underground gas storage facility, *Journal of Geophysical Research*, **124**, 8753-8770.